UC Santa Cruz
UC Santa Cruz Previously Published Works

Title

SDSS-IV MaNGA: How the Stellar Populations of Passive Central Galaxies Depend on Stellar and Halo Mass

Permalink

https://escholarship.org/uc/item/77f6c5hq

Journal

The Astrophysical Journal, 933(1)

ISSN

0004-637X

Authors

Oyarzún, Grecco A
Bundy, Kevin
Westfall, Kyle B
et al.

Publication Date

2022-07-01

DOI

10.3847/1538-4357/ac7048

Peer reviewed

SDSS-IV MaNGA: How the Stellar Populations of Passive Central Galaxies Depend on Stellar and Halo Mass

Grecco A. Oyarzún[1] , Kevin Bundy[2] , Kyle B. Westfall[2] , Jeremy L. Tinker[3] , Francesco Belfiore[4] ,
Maria Argudo-Fernández[5] , Zheng Zheng[6,7], Charlie Conroy[8] , Karen L. Masters[9] , David Wake[10] , David R. Law[11] ,
Richard M. McDermid[12] , Alfonso Aragón-Salamanca[13] , Taniya Parikh[14], Renbin Yan[15] , Matthew Bershady[16,17,18] ,
Sebastián F. Sánchez[19] , Brett H. Andrews[20] , José G. Fernández-Trincado[21], Richard R. Lane[22] , D. Bizyaev[23] ,
Nicholas Fraser Boardman[24], Ivan Lacerna[25,26], J. R. Brownstein[27] , Niv Drory[28] , and Kai Zhang[29]

[1] Astronomy Department, University of California, Santa Cruz, CA 95064, USA; goyarzun@ucsc.edu
[2] University of California Observatories—Lick Observatory, University of California, Santa Cruz, CA 95064, USA
[3] Center for Cosmology and Particle Physics, Department of Physics, New York University, New York, NY 10003, USA
[4] INAF—Osservatorio Astrofisico di Arcetri, Largo E. Fermi 5, I-50157, Firenze, Italy
[5] Instituto de Física, Pontificia Universidad Católica de Valparaíso, Casilla 4059, Valparaíso, Chile
[6] National Astronomical Observatories, Chinese Academy of Sciences, A20 Datun Road, Beijing, People's Republic of China
[7] CAS Key Laboratory of FAST, NAOC, Chinese Academy of Sciences, People's Republic of China
[8] Center for Astrophysics | Harvard & Smithsonian, 60 Garden Street, Cambridge, MA 02138, USA
[9] Departments of Physics and Astronomy, Haverford College, 370 Lancaster Avenue, Haverford, PA 19041, USA
[10] Department of Physics, University of North Carolina Asheville, One University Heights, Asheville, NC 28804, USA
[11] Space Telescope Science Institute, 3700 San Martin Drive, Baltimore, MD 21218, USA
[12] MQAAAstro Research Centre, Macquarie University, NSW 2109, Australia
[13] School of Physics & Astronomy, University of Nottingham, University Park, Nottingham, NG7 2RD, UK
[14] Max-Planck-Institut für extraterrestrische Physik, Giessenbachstrasse 1, D-85748 Garching bei München, Germany
[15] Department of Physics and Astronomy, University of Kentucky, 505 Rose Street, Lexington, KY 40506-0055, USA
[16] University of Wisconsin–Madison, Department of Astronomy, 475 N. Charter Street, Madison, WI 53706-1582, USA
[17] South African Astronomical Observatory, PO Box 9, Observatory 7935, Cape Town, South Africa
[18] Department of Astronomy, University of Cape Town, Private Bag X3, Rondebosch 7701, South Africa
[19] Instituto de Astronomía, Universidad Nacional Autónoma de México, A.P. 70-264, C.P. 04510, Mexico
[20] PITT PACC, Department of Physics and Astronomy, University of Pittsburgh, Pittsburgh, PA 15260, USA
[21] Instituto de Astronomía, Universidad Católica del Norte, Av. Angamos 0610, Antofagasta, Chile
[22] Centro de Investigación en Astronomía, Universidad Bernardo O Higgins, Avenida Viel 1497, Santiago, Chile
[23] Apache Point Observatory, P.O. Box 59, Sunspot, NM 88349, USA
[24] School of Physics and Astronomy, University of St Andrews, North Haugh, St Andrews KY16 9SS, UK
[25] Instituto de Astronomía y Ciencias Planetarias, Universidad de Atacama, Copayapu 485, Copiapó, Chile
[26] Millennium Institute of Astrophysics, Nuncio Monsenor Sotero Sanz 100, Of. 104, Providencia, Santiago, Chile
[27] Department of Physics and Astronomy, University of Utah, 115 S. 1400 E, Salt Lake City, UT 84112, USA
[28] McDonald Observatory, The University of Texas at Austin, 1 University Station, Austin, TX 78712, USA
[29] Lawrence Berkeley National Laboratory, 1 Cyclotron Road, Berkeley, CA 94720, USA

Abstract

We analyze spatially resolved and co-added SDSS-IV MaNGA spectra with signal-to-noise ratio $\sim$100 from 2200 passive central galaxies ($z \sim 0.05$) to understand how central galaxy assembly depends on stellar mass (M_*) and halo mass (M_h). We control for systematic errors in M_h by employing a new group catalog from Tinker and the widely used Yang et al. catalog. At fixed M_*, the strengths of several stellar absorption features vary systematically with M_h. Completely model-free, this is one of the first indications that the stellar populations of centrals with identical M_* are affected by the properties of their host halos. To interpret these variations, we applied full spectral fitting with the code alf. At fixed M_*, centrals in more massive halos are older, show lower [Fe/H], and have higher [Mg/Fe] with 3.5σ confidence. We conclude that halos not only dictate how much M_* galaxies assemble but also modulate their chemical enrichment histories. Turning to our analysis at fixed M_h, high-M_* centrals are older, show lower [Fe/H], and have higher [Mg/Fe] for $M_h > 10^{12}\,h^{-1}\,M_\odot$ with confidence $>4\sigma$. While massive passive galaxies are thought to form early and rapidly, our results are among the first to distinguish these trends at fixed M_h. They suggest that high-M_* centrals experienced unique *early* formation histories, either through enhanced collapse and gas fueling or because their halos were early forming and highly concentrated, a possible signal of galaxy assembly bias.

Unified Astronomy Thesaurus concepts: Early-type galaxies (429); Elliptical galaxies (456); Galaxies (573); Galaxy ages (576); Galaxy evolution (594); Galaxy stellar content (621); Quenched galaxies (2016); Galaxy abundances (574); Galaxy dark matter halos (1880); Galaxy environments (2029); Galaxy properties (615); Galaxy spectroscopy (2171)

1. Introduction

The historical debate over spheroidal galaxy formation pitted an in situ process (so-called "monolithic collapse"; e.g., Eggen et al. 1962; Larson 1974; Arimoto & Yoshii 1987; Bressan et al. 1994) against an ex situ one (so-called "hierarchical assembly"; e.g.,

Toomre 1977; White & Rees 1978). More recently, this debate has been recast in the form of a proposed "two-phase" scenario that incorporates elements from both formation pathways (Oser et al. 2010, 2012; Johansson et al. 2012b). The question now is, what physical processes, both in situ and ex situ, dominate, and at what redshifts?

The two-phase formation scenario found particular motivation and success in explaining why, since $z \sim 2$, the M_* of passive spheroidal galaxies has apparently increased by only a factor of two (Toft et al. 2007; Buitrago et al. 2008; Cimatti et al. 2008; van Dokkum et al. 2010), while their effective radii (R_e) have increased by a factor of three to six (Daddi et al. 2005; Trujillo et al. 2006a, 2006b, 2007; Zirm et al. 2007; van der Wel et al. 2008; van Dokkum et al. 2008; Damjanov et al. 2009; Cassata et al. 2010, 2011; van der Wel et al. 2014). After an initial phase that forms the "red nuggets" observed at $z \sim 2$ (van Dokkum et al. 2009; Newman et al. 2010; Damjanov et al. 2011; Whitaker et al. 2012; Dekel & Burkert 2014), the second evolutionary phase involves stellar accretion through minor mergers, which preferentially adds ex situ stars to the outskirts (e.g., Zolotov et al. 2009; Hopkins et al. 2010b; Tissera et al. 2013, 2014; Cooper et al. 2015; Rodriguez-Gomez et al. 2016). It has been shown that such accretion efficiently increases R_e while keeping M_* roughly constant (e.g., Bezanson et al. 2009; Barro et al. 2013; Cappellari et al. 2013; Wellons et al. 2016).

Direct support of this picture comes from studies of the surface brightness profiles of massive nearby galaxies that almost always feature multiple components (e.g., Huang et al. 2013a). Their inner parts ($R < 1$ kpc) are very compact and populate the same region of the mass−size plane as massive $z > 1$ galaxies (Huang et al. 2013b). In contrast, their outer envelopes can be quite extended ($R > 10$ kpc) and are consistent with being built through minor mergers (Huang et al. 2013b). These outer envelopes can also show greater ellipticity than the inner parts, potentially reflecting the orbital properties of accreted satellites (Huang et al. 2018).

In Oyarzún et al. (2019), we applied a different test of the two-phase formation scenario by searching for the predicted flattening of the stellar metallicity profile that is expected from the accretion of lower-mass galaxies (e.g., Cook et al. 2016; Taylor & Kobayashi 2017). Using a sample of early-type galaxies (ETGs) from the MaNGA survey (Bundy et al. 2015), we detected a flattening beyond R_e in the otherwise declining metallicity profiles. This flattening grows more prominent with increasing M_*, especially for ETGs with $M_* > 10^{11} M_\odot$. This observation suggests not only that massive ETGs assembled their outskirts through minor mergers but also that their ex situ stellar mass fraction is higher, in agreement with theoretical predictions (Rodriguez-Gomez et al. 2016).

With mergers and stellar accretion driving the second phase of spheroidal galaxy evolution, it is natural to search for a link between passive centrals and their host halo environments, given that those environments determine the central galaxy's merger history (e.g., Hopkins et al. 2010a). Unfortunately, searches for signatures of environment-driven growth in spatially resolved surveys have been so far inconclusive. Santucci et al. (2020) compared the stellar population gradients of central and satellite galaxies in the SAMI survey (Allen et al. 2015) at fixed M_* and found no significant differences. In initial efforts with MaNGA data, Zheng et al. (2017) and Goddard et al. (2017a, 2017b) studied the stellar age and metallicity gradients of massive galaxies and found no significant correlation with the local

environment or different proxies for the large-scale structure. The consensus of recent work is that at fixed M_* the stellar populations of massive galaxies within $\sim 1R_e$ are largely determined by their in situ formation histories rather than their environment (Peng et al. 2012; Greene et al. 2015; Goddard et al. 2017a; Scott et al. 2017; Contini et al. 2019; Bluck et al. 2020).

In this paper, we return to the important question of in situ versus ex situ evolution in passive galaxies. By adopting the perspective of the stellar-to-halo mass relation (SHMR), as defined for central galaxies (Moster et al. 2013), we reframe the question as a search for secondary correlations in the stellar populations of passive centrals as a function of halo mass (M_h) at fixed stellar mass (M_*), as well as correlations with M_* at fixed M_h. The first characterization allows us to revisit the role of environment, as expressed by M_h, in modulating galaxy formation at fixed M_*. The second lets us ask, to what extent does M_h determine the fate of a central galaxy?

The latter question is significant because theoretical models ultimately tie galaxy properties to their dark matter halos. Deviations, especially in the intrinsic scatter of the SHMR, have garnered a lot of interest and motivated work on "galaxy assembly bias," the possible existence of correlations between galaxy and secondary halo properties at fixed M_h (e.g., Zentner et al. 2014; Wechsler & Tinker 2018; Xu & Zheng 2020). According to the theory, galaxy luminosity correlates with halo formation time and concentration at fixed M_h (Croton et al. 2007; Matthee et al. 2017; Kulier et al. 2019; Xu & Zheng 2020). More concentrated halos, for example, facilitate the formation of deeper potential wells that may promote a more rapid assembly of M_* (Booth & Schaye 2010; Matthee et al. 2017; Kulier et al. 2019). Gas accretion and star formation should commence earlier in halos that formed early for their M_h (Kulier et al. 2019). Yet it remains unclear whether these predicted differences in halo and galaxy assembly history have an impact on the nature of the stellar populations across the SHMR as observed today.

To make progress on these questions and begin to delineate subtle secondary correlations between M_* and M_h, we construct an updated catalog of 2200 passive centrals drawn from the MaNGA survey. Previous work has emphasized the importance of $\sim 1\%$ level or better precision in measuring stellar age and abundances in ETG spectra (e.g., Conroy et al. 2014). Galaxy-integrated spectra in our sample can exceed signal-to-noise ratio (S/N) ~ 100 per galaxy, making MaNGA the premiere data set for co-added spectral analyses of nearby galaxies at this level of precision. The S/N from stacking all single-fiber ETG spectra in the Sloan Digital Sky Survey (SDSS) MAIN Galaxy Survey (York et al. 2000; Gunn et al. 2006; Alam et al. 2015) would be 0.6 times lower than the equivalent from the MaNGA stack. Equally important, the MaNGA data allow for simultaneous spatially resolved measurements, allowing for consistency checks across radial bins. Our high-S/N sample allows us to first detect subtle spectral differences in a model-free manner and then employ sophisticated full spectral fitting codes like `Prospector` and `alf` for the interpretation (Leja et al. 2017; Johnson et al. 2021; Conroy & van Dokkum 2012; Conroy et al. 2018). These codes model the nonlinear response of spectral features (Conroy 2013) to infer the age, abundance of various elements, and initial mass function (IMF) of old stellar systems ($\gtrsim 1$ Gyr), while also accounting for uncertainties in stellar evolution.

We also pay close attention to the impact of systematic errors on our results from potential biases in the M_h estimates. We are unfortunately limited in this study to halo estimates from

group-finding algorithms, which must first distinguish centrals from satellites and then require total M_* measurements of all group members (e.g., Yang et al. 2005, 2007). Group catalogs often fail to reproduce the fractions of red and blue satellites, the dependence of the SHMR for centrals on galaxy color, and correlations between M_h and secondary galaxy properties (Tinker 2020). We address these concerns by utilizing the new SDSS halo catalog in Tinker (2020, 2021), which exploits deep photometry from the DESI Legacy Imaging Survey (Dey et al. 2019). Tinker (2020) also implement a group-finding algorithm that is calibrated on observations of color-dependent galaxy clustering and estimates of the total satellite luminosity. As a result, their catalog better reproduces the color-dependent satellite fraction of galaxies and improves on the purity and completeness of central galaxy samples. In this work, we use the M_h estimates by Tinker (2020, 2021) and compare them against those by Yang et al. (2005, 2007), allowing us to assess how sensitive our results are to systematics in halo catalogs.

This paper is structured as follows. In Section 2, we introduce our data set and sample of passive central galaxies. In Section 3, we describe our treatment of the spectra and the stellar population fitting process. In Section 4, we show the results from direct spectral comparison and stellar population fitting. We interpret our findings in Section 5 and summarize in Section 6. Stellar masses throughout were obtained assuming a Kroupa (2001) IMF. The halo masses used in this work are reported in units of $h^{-1} M_\odot$. For all other physical quantities, this work adopts $H_0 = 70$ km s^{-1} Mpc^{-1}. All magnitudes are reported in the AB system (Oke & Gunn 1983).

2. Data Set

2.1. The MaNGA Survey

The MaNGA survey (Bundy et al. 2015; Yan et al. 2016a) is part of the now-complete fourth generation of SDSS (York et al. 2000; Gunn et al. 2006; Blanton et al. 2017; Aguado et al. 2019) and obtained spatially resolved spectra for more than 10,000 nearby galaxies ($z < 0.15$). By means of integral field unit spectroscopy (IFS; Drory et al. 2015; Law et al. 2015), every galaxy was observed with fiber bundles with diameters varying between 12″5 and 32″5 and composed of 19–127 fibers. The resulting radial coverage reaches between $1.5R_e$ and $2.5R_e$ for most targets (Wake et al. 2017). The spectra cover the wavelength range 3600–10300 Å at a resolution of $R \sim 2000$ (Smee et al. 2013). The reduced spectra have a median spectral resolution of $\sigma = 72$ km s^{-1}.

All MaNGA data used in this work were reduced by the Data Reduction Pipeline (DRP; Law et al. 2016, 2021; Yan et al. 2016b). The data cubes typically reach a 10σ continuum surface brightness of 23.5 mag arcsec^{-2}, and their astrometry is measured to be accurate to 0″1 (Law et al. 2016). Deprojected distances, stellar kinematics, and spectral index maps were calculated by the MaNGA Data Analysis Pipeline (DAP; Belfiore et al. 2019; Westfall et al. 2019). This work also used Marvin (Cherinka et al. 2019), the tool specially designed for access and handling of MaNGA data.[30]

Effective radii (R_e) for all MaNGA galaxies are publicly available as part of the NASA-Sloan Atlas[31] (NSA). These R_e were determined using an elliptical Petrosian analysis of the

r-band image from the NSA, using the detection and deblending technique described in Blanton et al. (2011).

2.2. Selection of Passive Galaxies

This paper is based on the MaNGA Product Launch 11 (MPL-11) data set, which consists of observations for over 10,000 MaNGA targets (see Table 1 in Law et al. 2021 for reference on the various release versions). To select passive galaxies, we used estimates of the spatially integrated specific star formation rate (sSFR) of MaNGA galaxies derived as part of the pipeline for the pipe3D Value-Added Catalog for DR17.[32] These sSFRs are based on measurements of the Hα equivalent width that were corrected by dust attenuation using the Balmer decrement (Sánchez et al. 2016). We defined our sample of passive galaxies by setting the criterion log(sSFR) < -11.5 $M_\odot$ yr^{-1}.

Our approach yielded a subset with 3957 passive galaxies, of which 2217 are identified as centrals in the catalog by Tinker (2020, 2021) and 952 in the Yang et al. (2007) and Wang et al. (2016) catalog. Details on the environmental classification are presented in Section 2.4.

2.3. Stellar Masses

To estimate the M_* of our galaxies, we first co-added the MaNGA spectra within the R_e of every galaxy (measured on r-band imaging from SDSS). Before co-addition, we shifted every spectrum back to the rest frame using the stellar systemic velocity (v_*) maps calculated by the DAP. Then, we estimated the mass within $1R_e$ by running the stellar population fitting code Prospector (Leja et al. 2017; Johnson et al. 2021) on the co-added spectrum. Our runs adopted the MILES stellar library (Sánchez-Blázquez et al. 2006), MIST isochrones (Dotter 2016; Choi et al. 2016), and Kroupa (2001) IMF. Further details on our Prospector runs are presented in Section 3.4.

We then assumed the total spectroscopic stellar mass of every galaxy to be

$$M_*^{\text{total}} = 2M_*^{R_e} \times 10^{-0.15}, \tag{1}$$

where $M_*^{R_e}$ is the spectroscopic stellar mass within the effective radius measured with Prospector. Since it has been found that half-mass radii are smaller than half-light radii (García-Benito et al. 2017), our M_*^{total} may be overestimated. Yet we do not expect any biases to arise from this definition, since differences between half-mass and half-light radii have not been found to correlate with stellar mass (Szomoru et al. 2013). Any overestimation of our stellar masses was corrected by implementing an offset of 0.15 dex (see the multiplicative term in the equation). This value was obtained by measuring the offset between our $2M_*^{R_e}$ and the stellar masses measured through k-correction fits to the Sérsic fluxes in the NSA (Blanton & Roweis 2007). For the rest of the paper, we will simply refer to M_*^{total} as M_*.

2.4. Yang+Wang Halo Masses

For our first characterization of environment, we used the MPL-9 version of the Galaxy Environment for MaNGA Value-
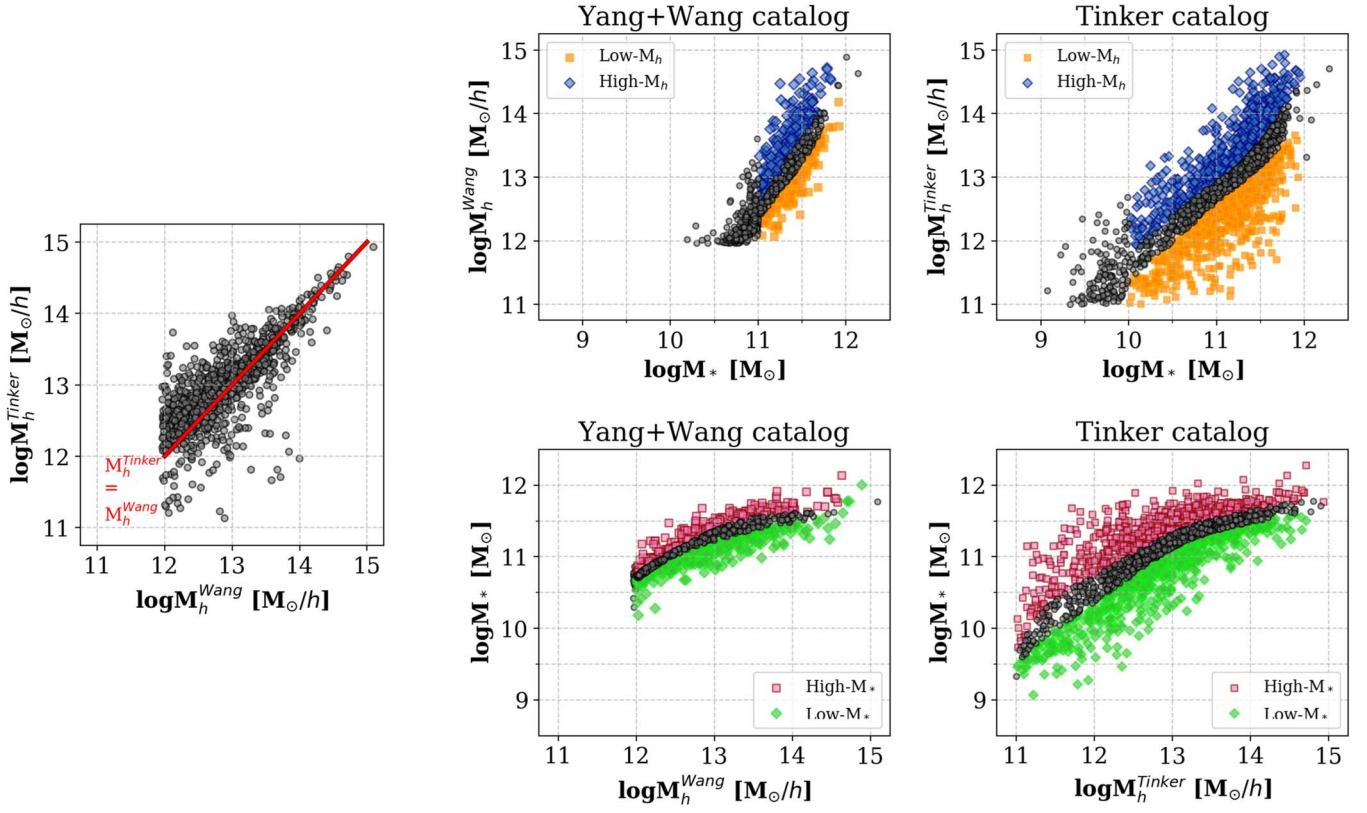

Figure 1. Comparison between the M_h measured by Wang et al. (2016) and Tinker (2021) for our passive centrals. The $M_h^{\text{Wang}} = M_h^{\text{Tinker}}$ line is shown in red. Right: SHMR for passive centrals in the two catalogs. We define our subsamples based on the independent property and SHMR. At fixed M_* (top panels), high-M_h centrals are shown in blue and low-M_h centrals in orange. At fixed M_h (bottom panels), high-M_* centrals are shown in red and low-M_* centrals in green. Galaxies in regions of the SHMR with narrow dynamic range were not included in the analysis (gray). We also excluded galaxies between the 33rd and 66th percentiles in M_*-to-M_h ratio.

Added Catalog[33] (GEMA-VAC; Argudo-Fernández et al. 2015). We used this catalog to identify central galaxies and retrieve estimates of their halo masses. The environmental classification and halo mass entries were computed by cross-matching MaNGA MPL-9 with the Yang et al. (2007) group catalog for SDSS (see also Yang et al. 2005). The halo masses computed by Yang et al. (2007) assumed a WMAP3 cosmology (Spergel et al. 2007). In this work, we use the values in the GEMA-VAC that were updated to a WMAP5 cosmology (Dunkley et al. 2009) as part of the work by Wang et al. (2009, 2012, 2016).

The group catalog by Yang et al. (2007) was computed on the SDSS New York University Value-Added Galaxy Catalog (NYU-VAGC; Blanton et al. 2005) based on SDSS DR4 (Adelman-McCarthy et al. 2006). To compute the Yang et al. (2007) catalog, a series of steps were iterated until convergence was achieved. First, clustering analysis in redshift space was used to find potential cluster centers and groups. In the second step, group luminosities ($L_{19.5}$) were computed as the combined luminosity of all group members with $M_r - 5\log h \leqslant -19.5$ (hence the subscript in $L_{19.5}$). Dark matter halo masses, sizes, and velocity dispersions were then estimated. In particular, tentative M_h were assigned according to the $L_{19.5}$–M_h relation measured in the previous iteration, which assumes a one-to-one correspondence between $L_{19.5}$ and M_h. Finally, membership probabilities in redshift space around group centers were estimated. This allowed

for group memberships to update. The process from the second to the final step was repeated until no further changes in group memberships were observed. After convergence, final M_h were derived through abundance matching using the van den Bosch et al. (2007) halo mass function.

Of the 3957 passive galaxies in our sample, 952 are centrals with halo mass measurements in the GEMA-VAC (see Figure 1). The SHMR using the stellar masses from Section 2.3 and the halo masses from the Yang+Wang catalog are plotted in Figure 1. Details on the number of galaxies as a function of M_* and M_h are shown in Table 1.

2.5. Tinker Halo Masses

Group-finding algorithms, like the one described in Section 2.4, are affected by several issues. By not breaking down galaxy samples into star-forming and quiescent sub-samples, they can fail to reproduce the fraction of quenched satellite galaxies and misestimate by an order of magnitude M_h (Campbell et al. 2015). Some of these shortcomings can be tackled by calibrating the free parameters of the group finder with real data instead of mock catalogs. In this paper, we work with the group finder by Tinker (2020), which uses observations of color-dependent galaxy clustering and total satellite luminosity for calibration.

In the self-calibrating halo-based galaxy group finder by Tinker (2020), the probability of a galaxy being a satellite depends on galaxy type and luminosity. This dependence is quantified by 14 different parameters that are calibrated until

---

[33] https://www.sdss.org/dr15/data_access/value-added-catalogs/?vac_id = gema-vac-galaxy-environment-for-manga-value-added-catalog

Table 1
Number of Central Galaxies per Sample

$M_*[M_\odot] =$	$10^{10} - 10^{10.5a}$	$10^{10.5} - 10^{11a}$	$10^{11} - 10^{11.5}$	$10^{11.5} - 10^{12}$	Out of Range	Total
Yang+Wang	7	267	523	153	2	952
Yang+Wang low-M_h	0	0	174	48	⋯	222
Yang+Wang high-M_h	0	0	172	51	⋯	223
Tinker	211	514	948	412	132	2217
Tinker low-M_h	70	188	317	128	⋯	703
Tinker high-M_h	70	143	353	148	⋯	714
$M_h[M_\odot/h] =$	$10^{11} - 10^{12a}$	$10^{12} - 10^{13}$	$10^{13} - 10^{14}$	$10^{14} - 10^{15}$	Out of Range	Total
Yang+Wang	27	517	358	49	1	952
Yang+Wang low-M_*	0	170	120	19	⋯	309
Yang+Wang high-M_*	0	172	113	15	⋯	300
Tinker	329	888	860	139	1	2217
Tinker low-M_*	109	297	265	45	⋯	716
Tinker high-M_*	112	310	301	50	⋯	773

Note.
[a] These bins were not considered as a result of the narrow dynamic ranges in M_h or M_* (Figure 1).

the best-fitting model is found. First, a starting value for the parameters is adopted and the group finder is run until the fraction of red and blue satellites match the input data set. The assigned groups and halo masses are then used to populate the Bolshoi–Planck simulation (Klypin et al. 2016) and predict galaxy clustering and the total satellite luminosity. These predictions are compared to observational measurements to quantify the adequacy of the model. The process is then repeated until the best-fitting model is found.

This algorithm was applied to SDSS galaxies in Tinker (2021). Compared to the data set available to Yang et al. (2005, 2007), Tinker (2021) had access to deeper photometry from the DESI Legacy Imaging Survey (DLIS; Dey et al. 2019). This is quite important, since good accounting of group and galaxy M_* is key to properly constraining M_h (Bernardi et al. 2013; Wechsler & Tinker 2018). As a result, the SDSS group catalog by Tinker (2021) is an improvement in both data set and algorithm.

Despite improvements, the approach by Tinker (2020) still has limitations. Like all group-finding algorithms, it is susceptible to central galaxy misidentification. It also assumes that the amount of light in satellite galaxies is a function of halo mass only, and its implementation on SDSS data fails to match the clustering of faint quiescent galaxies (Tinker 2021). There is also room for further freedom in how the algorithm fits the data, in particular for taking into account secondary correlations between galaxy and halo properties (Tinker 2021).

The self-calibrating halo-based galaxy group finder applied to SDSS is publicly available.[34] We downloaded the catalog and cross-matched with our sample of quenched systems. We selected all galaxies with satellite probabilities lower than 0.1 and obtained a sample with 2217 passive central galaxies (see Table 1). The M_h measured by Tinker and Yang+Wang are compared in the left panel of Figure 1. The right panel shows the SHMR using our M_* and $M_h^{\rm Tinker}$, which extends down to $M_* \sim 10^{10}\ M_\odot$ ($M_h^{\rm Tinker} \sim 10^{11}\ h^{-1}\ M_\odot$). Figure 2 shows that the average number of satellites per halo monotonically increases with $M_h^{\rm Tinker}$.
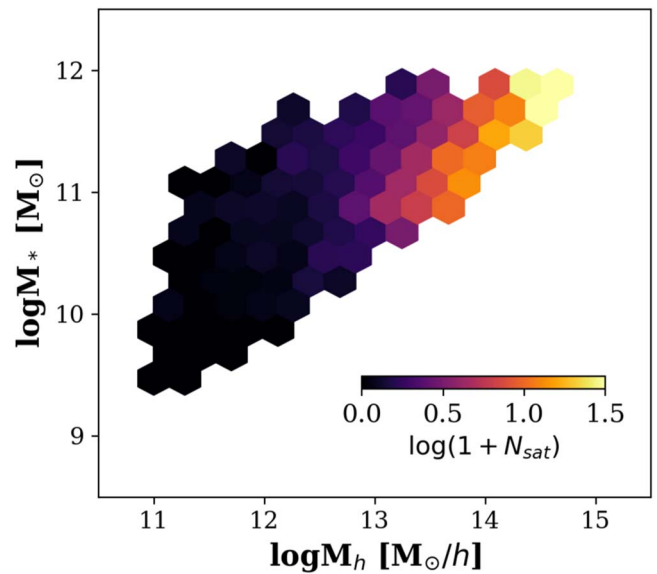

Figure 2. Number of satellite galaxies per halo as a function of M_h and M_* in the Tinker (2020, 2021) catalog. At fixed M_*, centrals in high-M_h halos tend to have more satellites than centrals in low-M_h halos.

3. Methodology

3.1. Sample Definitions

The correlation between the M_* and M_h of central galaxies has significant scatter, some of which is thought to be intrinsic (e.g., Xu & Zheng 2020). This would imply that the stellar masses of central galaxies are determined not uniquely by the mass of their halos but also by secondary properties (e.g., Zentner et al. 2014). In consequence, the SHMR is a very useful tool for testing the mechanisms driving the galaxy–halo connection (e.g., Leauthaud et al. 2017). The purpose of this work is to probe these mechanisms through the analysis of galaxy stellar populations.

Figure 1 shows the SHMR for our sample of centrals according to both environmental catalogs. We computed the 33rd and 66th percentiles in M_*-to-M_h ratio as a function of M_* to define two subsamples. High-M_h centrals are those that

---
[34] https://galaxygroupfinder.net

reside in high M_h for their M_* and are shown in blue. Low-M_h centrals, on the other hand, reside in low-M_h halos for their M_* and are shown in orange. In equation form,

$$\text{High} - M_h \text{ sample:} \quad \frac{M_*}{M_h}(M_*) < \left[\frac{M_*}{M_h}(M_*)\right]_{.33}, \qquad (2)$$

$$\text{Low} - M_h \text{ sample:} \quad \frac{M_*}{M_h}(M_*) > \left[\frac{M_*}{M_h}(M_*)\right]_{.66}. \qquad (3)$$

To quantify correlations at fixed M_h, we also computed the 33rd and 66th percentiles in M_*-to-M_h ratio as a function of M_h. High-M_* centrals have high M_*-to-M_h ratios, whereas low-M_* centrals have low M_*-to-M_h ratios. Put in an equation,

$$\text{High} - M_* \text{ sample:} \quad \frac{M_*}{M_h}(M_h) > \left[\frac{M_*}{M_h}(M_h)\right]_{.66}, \qquad (4)$$

$$\text{Low} - M_* \text{ sample:} \quad \frac{M_*}{M_h}(M_h) < \left[\frac{M_*}{M_h}(M_h)\right]_{.33}. \qquad (5)$$

Galaxies between the 33rd and 66th percentiles in M_*-to-M_h ratio were not used and are shown as gray points in Figure 1. Since the distribution of centrals in M_*-to-M_h ratio as a function of M_* or M_h is rather flat, no subsample is biased as a result of uncertainties in M_* or M_h. Note that the sample membership of a given galaxy depends on the environmental catalog, since our classification scheme is based on M_h. The number of galaxies in every M_* and M_h bin for the two environmental catalogs is presented in Table 1. Due to the narrow dynamic range in M_h with the Yang+Wang catalog for $M_* < 10^{11} M_\odot$, the corresponding bins were not included in the analysis (see Table 1). The average number of satellites per halo (N_{sat}) for every subsample is plotted in Figure 2. At fixed M_*, N_{sat} correlates with M_h.

3.2. Co-addition and Stacking of Spectra

The spectral precision needed by our stellar population analysis requires high-S/N ($\gtrsim 50$) spectra (e.g., Conroy et al. 2014). Thus, we first co-added the MaNGA spectra within every galaxy following a radial binning scheme. We then computed the median of these co-additions to generate galaxy stacks for every subsample. The co-addition and stacking steps are described below.

For every galaxy, we associated galactocentric distances all spaxels by retrieving elliptical polar radii (R) from the DAP that account for the axis ratio of every object. We binned all the spaxels within every galaxy into the three annuli $R = [0, 0.5]R_e$, $[0.5, 1]R_e$, and $[1, 1.5]R_e$. After masking sky-line residuals and spectra outside the wavelength range (3700 Å, 9200 Å) in the observed frame, the co-added spectra in every bin were co-added. To do this, we shifted every spectrum back to the rest frame using the stellar systemic velocity (v_*) maps computed by the DAP with a Voronoi binning scheme that aims for a minimum S/N of 10 bin^{-1}. We did not convolve the spectra to a common σ_* prior to stacking. We also masked all spaxels that were flagged as unusable by the DRP and DAP.

After co-addition, we ran pPXF (Cappellari & Emsellem 2004; Cappellari 2017) with the MILES Single Stellar Population (SSP) library (Vazdekis et al. 2010) on the resulting spectra to measure the co-added v_* and σ_*. Co-added v_* showed values $v_* \lesssim 1$ km s^{-1}, indicating that spectra were

properly shifted back to the rest frame. We also ran Prospector (details in Section 3.4) to measure stellar mass surface density profiles for every galaxy.

After binning in M_* and M_h (see Table 1), we stacked the spectra across every subsample in each of the four radial annuli. For stacking, all co-added spectra were convolved to $\sigma_* = 350$ km s^{-1} and median normalized. This value is motivated by the maximum observed dispersion, and it mitigates line-strength variations caused by different Doppler broadening. Stacks were obtained by computing the median at each wavelength after removing the continuum. Errors on the stacks were quantified through Monte Carlo simulations of the stacking process that took into account the propagated errors. Two stacked spectra are shown in Figure 3 after all emission lines were masked. The dependence of the stacks on whether masking is performed before or after stacking is minimal.

The Appendix shows stacked spectra at multiple radii and M_h. We typically reach S/N > 200 at the centers and S/N > 100 in the outskirts. We find the spectral S/N of the stacks to show dependence on both the individual S/N and the total number of spectra. As a result, the highest M_* and M_h stacks show the lowest spectral S/N of all bins by factors of ~ 2.

3.3. Evidence for Environmental Differences

The top panel of Figure 3 compares the stacked spectra at the centers of high- and low-M_h centrals with $M_* = 10^{10} - 10^{10.5}$ $M_\odot$. With M_* held constant (see Section 3.1), any differences between the spectra in this comparison can be interpreted as environmental signatures. In this subsection, we describe our method for finding and highlighting these signatures.

We started by subtracting high-M_h stacks from low-M_h counterparts of the same M_*. An example of the resulting spectral difference is shown in the middle panel of Figure 3. Then, to highlight variations in spectral features, we subtracted fits from the spectral differences. The result is shown in the bottom panel of Figure 3. Note how the spectral difference captures variations in both spectral shape and features. As we will show in Section 4, we find some significant environmental signatures at different M_* and radii. This is evidence that M_h has an impact on the stellar populations of passive central galaxies at fixed M_*.

For context, some abundance-sensitive features are labeled in this figure. Differences at these locations highlight the fact that environmental signatures can manifest because of differences in stellar age, metallicity, element abundances, and the IMF of central galaxies (Conroy et al. 2018). To inform our interpretation of these differences, we turned to stellar population fitting codes Prospector and alf.

3.4. Stellar Mass Surface Density Profiles with Prospector

We used the stellar population fitting code Prospector[35] (Leja et al. 2017; Johnson et al. 2021) on the co-added spectra to estimate stellar masses (Section 2.3) and stellar mass surface density (Σ_*) profiles for all galaxies.

Prospector samples the posterior distribution for a variety of stellar population parameters and star formation history (SFH) prescriptions defined by the user. In this code, stellar population synthesis is handled by the code FSPS[36]

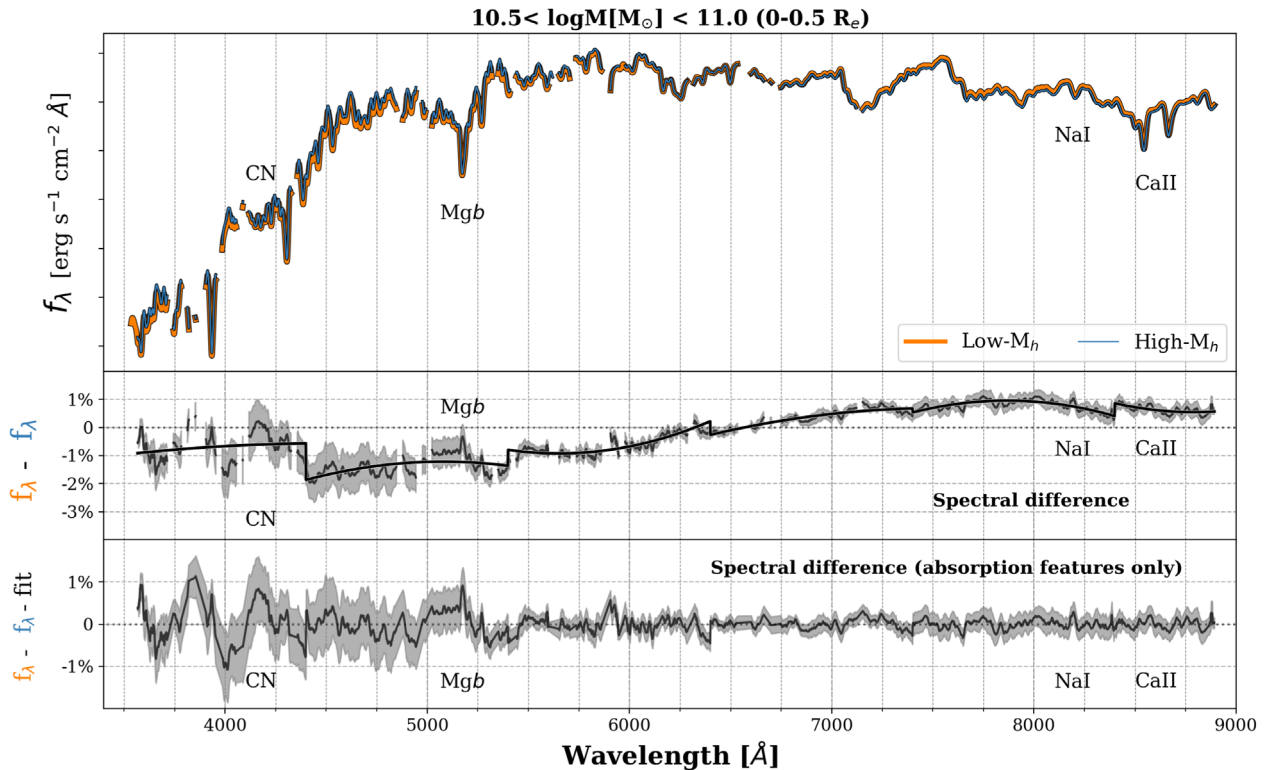[35] https://github.com/bd-j/prospector/blob/master/doc/index.rst
[36] https://github.com/cconroy20/fsps

Figure 3. Top: stacked spectra of central galaxies at fixed M_* that reside in low-M_h halos (orange) and high-M_h halos (blue). The data represent stacks within the central $0.5R_e$ for $M_* = 10^{10.5} - 10^{11}\ M_\odot$ centrals. Middle: the high-M_h stack subtracted from the low-M_h stack with a fit plotted in black. Gray shading shows the error on this difference. Bottom: result of subtracting the fit from the spectral difference. This highlights variations in several absorption features, some of which help to break degeneracies between various stellar population parameters. The two subsets reveal significant differences in both spectral shape and absorption features. Requiring no model assumptions, this figure demonstrates that M_h has an impact on the stellar populations of passive central galaxies with the same M_*.

(Conroy et al. 2009; Conroy & Gunn 2010). Our runs used the MILES stellar library (Sánchez-Blázquez et al. 2006), MIST isochrones (Dotter 2016; Choi et al. 2016), and Kroupa IMF (Kroupa 2001) as inputs. We adopted a nonparametric SFH with a continuity prior, which emphasizes smooth SFHs over time (Leja et al. 2019). As in Leja et al. (2019), we used the following time bins:

$$
\begin{aligned}
0 < t &< 30\ \mathrm{Myr}, \\
30\ \mathrm{Myr} < t &< 100\ \mathrm{Myr}, \\
100\ \mathrm{Myr} < t &< 330\ \mathrm{Myr}, \\
330\ \mathrm{Myr} < t &< 1.1\ \mathrm{Gyr}, \\
1.1\ \mathrm{Gyr} < t &< 3.6\ \mathrm{Gyr}, \\
3.6\ \mathrm{Gyr} < t &< 11.7\ \mathrm{Gyr}, \\
11.7\ \mathrm{Gyr} < t &< 13.7\ \mathrm{Gyr}.
\end{aligned}
\tag{6}
$$

Our parameter space also included the optical depth of dust in the V band (Kriek & Conroy 2013), stellar mass, stellar velocity dispersion, and mass-weighted stellar ages and metallicities. To derive the posterior distributions, we used the Dynamic Nested Sampling package dynesty[37] (Speagle 2020).

3.5. Stellar Ages and Element Abundances with alf

We used the program alf to characterize the stellar populations in more detail. This code fits the absorption-line optical–near-infrared spectrum of old ($\gtrsim$1 Gyr) stellar systems

(Conroy & van Dokkum 2012; Conroy et al. 2018). Unlike Prospector, alf allows us to fit for the abundances of multiple elements and the IMF. This comes at the cost of computation times that are longer by a factor of 100. alf is based on the MIST isochrones (Dotter 2016; Choi et al. 2016) and the empirical stellar libraries by Sánchez-Blázquez et al. (2006) and Villaume et al. (2017). Full spectral variations induced by deviations from the solar abundance pattern are quantified in the theoretical response functions (Conroy et al. 2018; Kurucz 2018). These allow alf to sample a multivariate posterior that includes the abundances of 19 elements (including C, N, O, Mg, and Fe).

We ran alf in "full" mode, which fits for a two-component SFH, stellar velocity dispersion, IMF, and the abundances of 19 elements. We adopted a triple power-law IMF with two free parameters. Power laws were fit in the ranges 0.08–0.5 $M_\odot$ and 0.5–1 $M_\odot$. The IMF slope was set to -2.35 in the range 1–100 $M_\odot$ (Salpeter 1955). Posterior sampling was performed with emcee (Foreman-Mackey et al. 2013). We found our runs to fully converge under the default configuration, which is 1024 walkers, 10^4 burn-in steps, and 100-step chains. For this setup, alf took $\sim$100 CPU hours per spectrum to run.

With alf, we recover stellar velocity dispersions within 1% of the input value ($\sigma_* = 350$ km s^{-1}). We derived mass-weighted stellar ages by mass-weighting the posteriors of the two-component SFHs. The stellar ages measured by Prospector and alf show agreements within 2 Gyr. The most significant age differences between high- and low-M_h centrals are found by both codes. More subtle differences are only detected by alf (more details in Section 4). Following the

---

[37] https://github.com/joshspeagle/dynesty/blob/master/docs/source/index.rst

approach of Lick indices, we use [Mg/Fe] as a proxy for [α/Fe] throughout (Johansson et al. 2012a; see Kirby et al. 2008 for other elements that can be used as tracers for [α/Fe]). Conversions from [X/H] to [X/Fe] assumed the correction factors in Schiavon (2007). The abundances measured by alf cannot be directly compared to the stellar metallicity reported by Prospector, since the latter only fits a scaled solar abundance pattern.

For estimating uncertainties on the fitted parameters, we adopted a three-step method that was iterated over 5 times. First, we bootstrapped the galaxies selected in the sample assignment step from Section 3.1. Then, we computed the stacked spectra for the corresponding bootstrapped galaxies as in Section 3.2. Lastly, we fit each stacked spectrum with alf. This resulted in five posterior distributions for every subsample in each stellar and halo mass bin. The five distributions were then folded in, such that the final posteriors account for uncertainties in both methodology and modeling. Some of the model fits and posterior distributions are shown in the Appendix.

4. Results

4.1. Empirical Spectral Differences with Environment

Using the methods in Section 3.3, we quantified differences between the spectra of centrals in high- and low-M_h halos. Our findings are plotted in Figure 4. The M_* of the compared galaxies increases from left to right, with the top row displaying results for an inner bin of galactocentric radius and the bottom row results for an outer bin. Shaded contours show 1σ errors, which fully account for uncertainties in sample assignment and stacking. Absorption features that are deeper in low-M_h galaxies are negative, whereas features that are stronger in high-M_h galaxies are positive. We listed the stellar parameters that drive feature changes as quantified in the response functions by Conroy et al. (2018).

At all M_* and radii, high-M_h centrals show stronger Mgb $\lambda5172$ absorption (Faber & Jackson 1976; Faber et al. 1985). Apart from being dominated by magnesium abundance, this spectral feature is also sensitive to iron enrichment. Another significant set of spectral differences are found around 4000 Å, which tend to be stronger in high-M_h centrals. These features are in a Ca-sensitive spectral region, as evidenced by the widely used Ca H and K, Ca $\lambda4227$, and Ca $\lambda4455$ spectral indices (e.g., Worthey et al. 1994; Tripicco & Bell 1995). Apart from being sensitive to the calcium abundance, features at these wavelengths are also sensitive to stellar age and overall metallicity.

The detection of these differences demonstrates that halos have an impact on the stellar populations of passive central galaxies that is secondary to the correlation between M_h and M_*. We now turn to our results from stellar population fitting to attempt to interpret these results.

4.2. Integrated Measurements

To derive the mean stellar population properties within the galaxy, we averaged the radial profiles derived with alf (Section 3.5). The results are shown with M_* and M_h as the controlling variable in the top and bottom panels of Figure 5, respectively. Measurements that used the Tinker catalog are plotted in circles, whereas those that used the Yang+Wang catalog are shown in the insets as triangles.

To first order, it is well known that stellar age and metallicity increase with the M_* or central velocity dispersion of galaxies (Faber & Jackson 1976; Cid Fernandes et al. 2005; Gallazzi et al. 2005; Thomas et al. 2005, 2010; González Delgado et al. 2014; McDermid et al. 2015). While the top row of Figure 5 confirms this trend with age for the passive central galaxies in our study, we see that [Fe/H] decreases with M_*. In the literature, the word "metallicity" refers to a weighted average of the abundance of various elements (i.e., a rescaling of the solar abundance pattern), whereas the [Fe/H] measurements that we derived with alf map the abundance of iron only. The decrease in [Fe/H] with M_* for $M_* > 10^{11}$ $M_\odot$ is likely the result of how the formation timescales of galaxies become more rapid as M_* increases.

The plot in the top row, second column compares the stellar ages of low- and high-M_h centrals at fixed M_*. With the Tinker catalog, we find low-M_h centrals to be younger than high-M_h counterparts by $\sim 1 - 2$ Gyr. Differences between the [Fe/H] of low- and high-M_h centrals are also present, with high-M_h centrals showing lower [Fe/H] by $\lesssim 0.05$ dex at all M_*. High-M_h centrals also show slightly greater [Mg/Fe], especially for $M_* > 10^{11}$ $M_\odot$. Figure 5 shows that the deeper absorption seen in high-M_h centrals (Figure 4) is primarily a result of their older ages and higher magnesium enhancement.

We can assign confidence levels to these results by computing the Bayes factor. As an example, we can consider the following two hypotheses: either high-M_h centrals are older, or low-M_h centrals are older. The Bayes factor is just the ratio between the marginalized likelihoods of the models since we are interested in adopting flat, uninformative priors. In equation form, the Bayes factor is equal to

$$\mathcal{B} = \prod_{M_*} B_i = \prod_{M_*} \frac{\mathrm{IP}(\mathrm{age}_{\mathrm{high}-M_h} - \mathrm{age}_{\mathrm{low}-M_h} > 0)}{\mathrm{IP}(\mathrm{age}_{\mathrm{high}-M_h} - \mathrm{age}_{\mathrm{low}-M_h} < 0)}. \quad (7)$$

Figure 5 indicates that for the first M_* bin the stellar ages of the two subsamples are quite similar, and therefore $\mathcal{B}_1 \sim 1$. On the other hand, high-M_h centrals are significantly older in the highest-M_* bin, and hence the associated Bayes factor is $\mathcal{B}_4 \sim 100$. If we assume that the two hypotheses cover all possible model options (i.e., that at least one of the subsamples is older), we can impose that the sum of the model probabilities is equal to 1 (e.g., Oyarzún et al. 2017). With this method, we conclude that high-M_h centrals are older, have lower [Fe/H], and feature higher [Mg/Fe] than low-M_h centrals with 3.6σ, 3.6σ, and 3.4σ confidence levels, respectively.

We can now invert this analysis and use M_h as the controlling variable. The results are shown in the bottom row of Figure 5 and indicate clear secondary behavior in the stellar population of galaxies with different values of M_* at fixed M_h. We see that high-M_* centrals are nearly always older. For $M_h > 10^{12}$ h^{-1} $M_\odot$, this difference can exceed 2 Gyr, has a significance of 4.4σ, and is clear in both halo catalogs. Differences in [Fe/H] show more complicated behavior that is dependent on M_h. For $M_h < 10^{12}$ h^{-1} $M_\odot$, high-M_* centrals show higher [Fe/H] by as much as 0.2 dex (8σ). For $M_h > 10^{12}$ h^{-1} $M_\odot$, the difference reverses and [Fe/H] decreases with M_h (5σ). Significant differences are also observed in [Mg/Fe], with high-M_* centrals showing greater [Mg/Fe] at all M_h (5.6σ) and for $M_h > 10^{12}$ h^{-1} $M_\odot$ (4.4σ) with both catalogs.

To help visualize the results across this multidimensional space, Figure 6 shows the SHMR colored by each of the stellar population properties we considered. This figure was made by
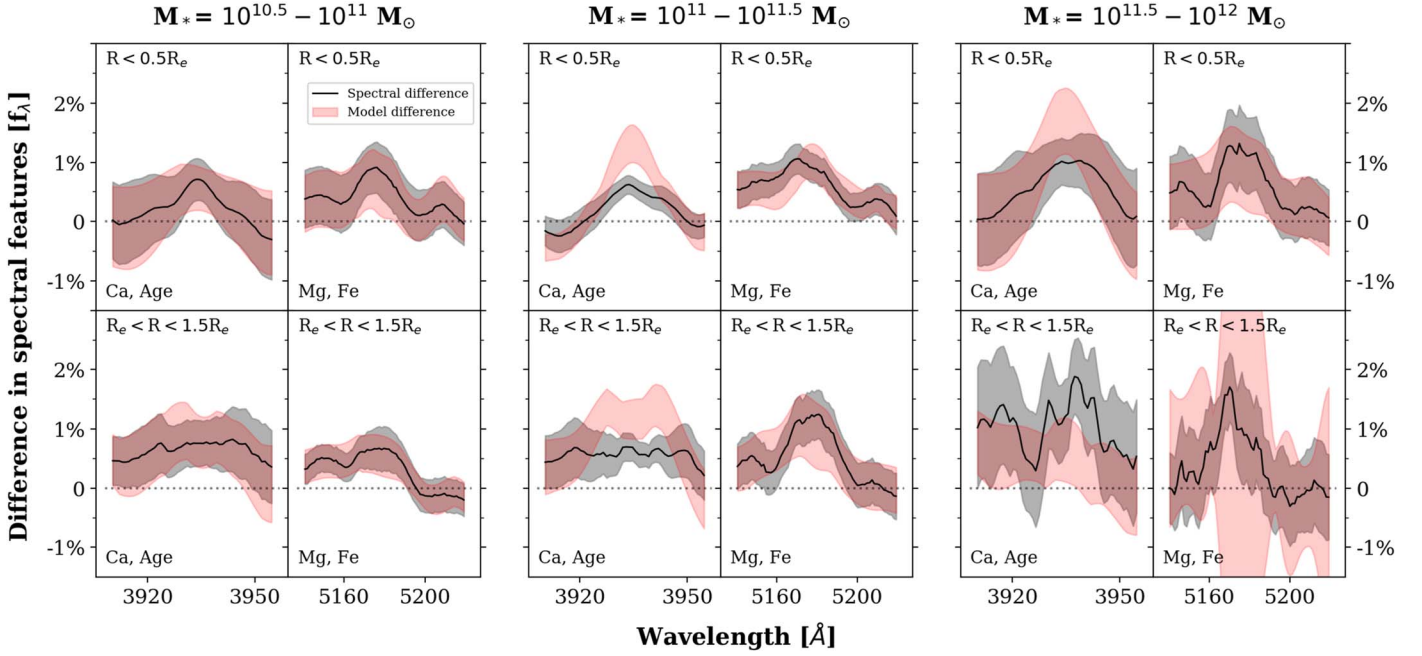
Figure 4. Differences in spectral features between low- and high-M_h centrals of the same M_*. Positive difference indicates stronger absorption in high-M_h galaxies, with the 1σ error plotted in gray. Different panels show different spectral features for which we detect significant differences that are systematic with M_* and radius. Stellar mass increases from left to right, galactocentric distance from top to bottom. Annotated are the stellar population parameters that dominate the strength of each feature. The red shading represents the 1σ posterior distribution of the best-fitting model spectra produced by alf. The alf posteriors reproduce the observed spectral differences well, although some model mismatch at the 1% level is apparent.
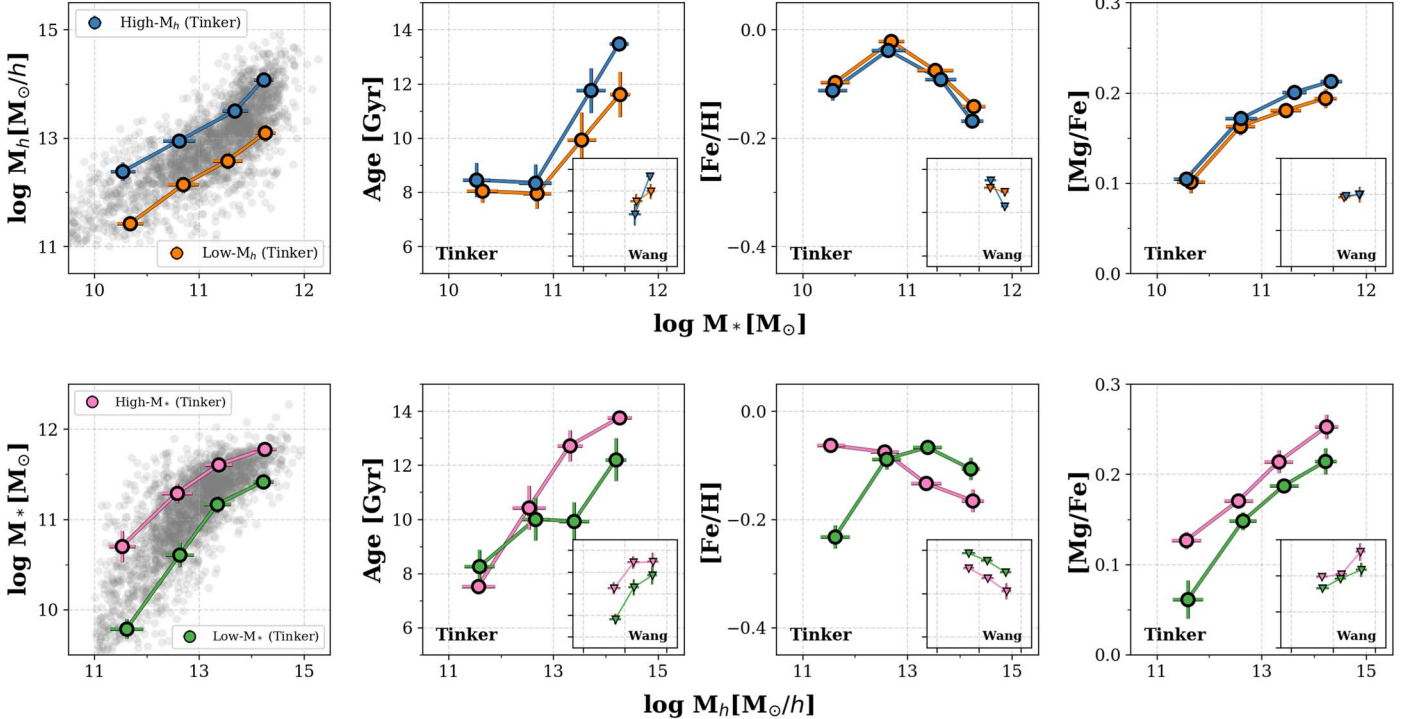
Figure 5. Stellar population parameters of passive central galaxies within $1.5R_e$ as a function of M_* (top) and M_h (bottom). Measurements that used the Tinker catalog for sample assignment are plotted in circles. Measurements that used the Yang+Wang catalog are shown in triangles. The stellar populations of passive centrals better correlate with M_* than with M_h. Top: high-M_h centrals are older (3.6σ), have lower [Fe/H] (3.6σ), and show higher [Mg/Fe] (3.4σ) than low-M_h centrals. Bottom: for $M_h > 10^{12}\ h^{-1}\ M_\odot$, the stellar populations of high-M_* centrals are older (4.4σ), have lower [Fe/H] (5σ), and have greater [Mg/Fe] (4.4σ) than those of low-M_* counterparts.

fitting a two-dimensional, second-degree polynomial in M_*–M_h space to the results from Figure 5. Note how stellar age and [Mg/Fe] vary not only with M_* but also with M_h. On the other hand, [Fe/H] depends almost exclusively on M_*.

4.3. The Stellar Population Profiles of Central Galaxies

We now look at the radial dependence of our derived measurements. The stellar population profiles at fixed M_* are
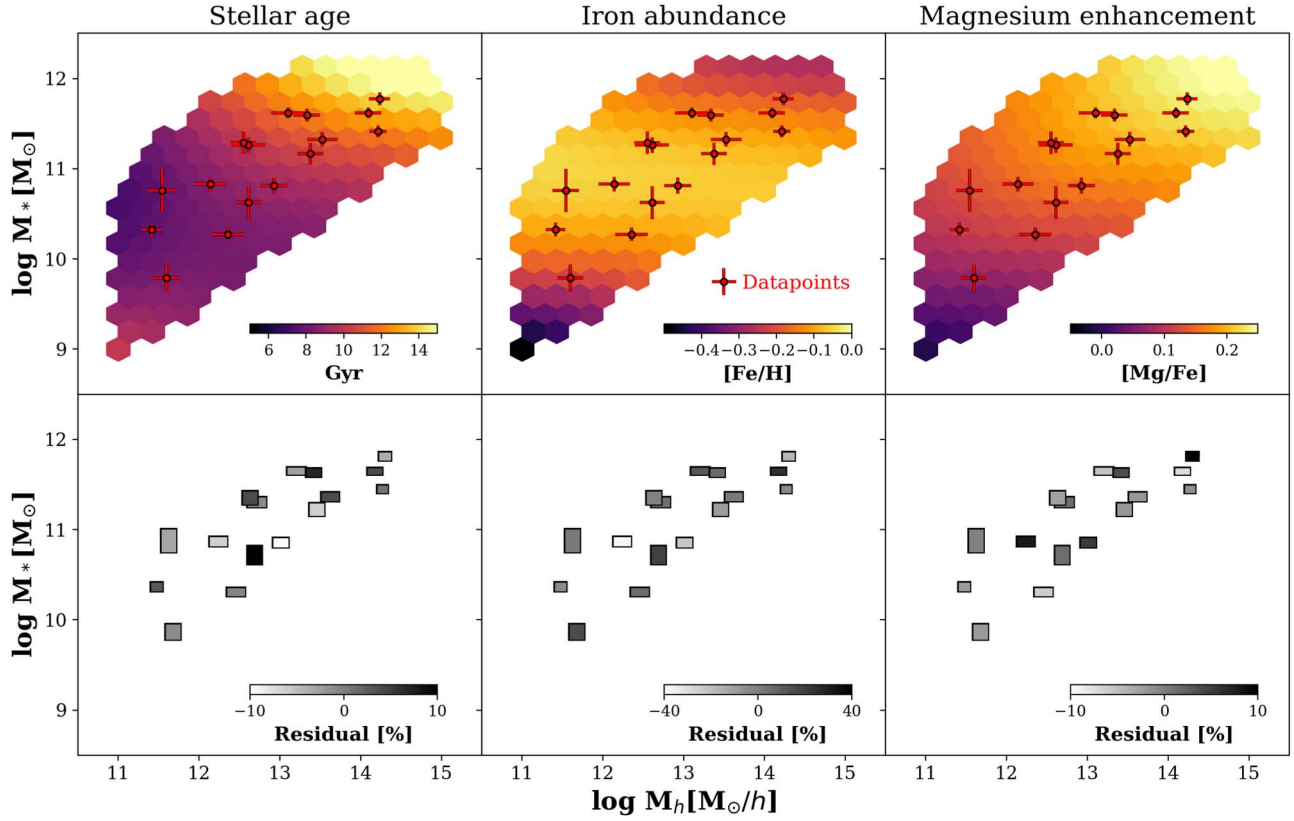
Figure 6. Top: the SHMR of passive centrals colored by stellar age, [Fe/H], and [Mg/Fe]. Values were derived by fitting two-dimensional polynomials in M_*–M_h space to the measurements from Figure 5 that adopted M_h^{Tinker} (red data points). All parameters depend on both M_* and M_h. Bottom: residuals relative to the median value of the parameter in the SHMR.
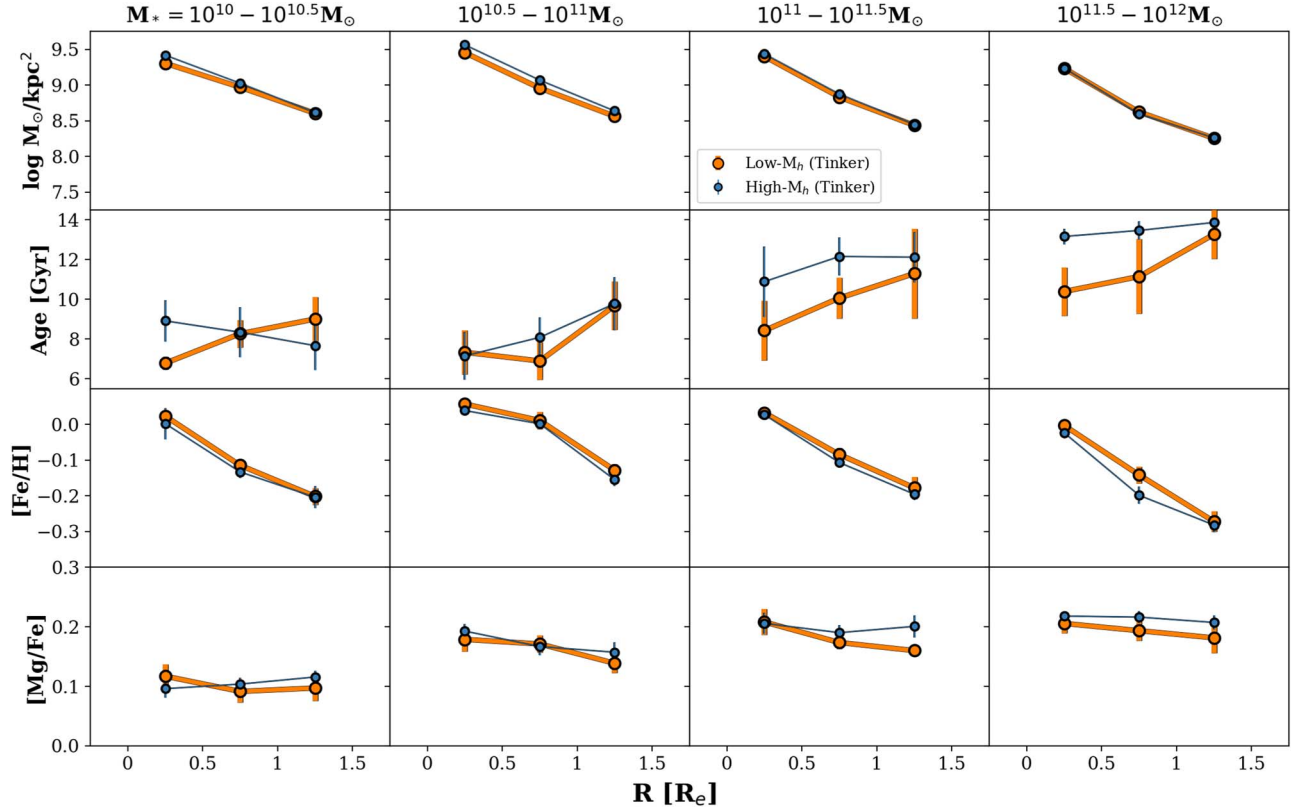
Figure 7. Stellar population profiles of low-M_h (orange) and high-M_h (blue) centrals at fixed M_* with the Tinker catalog. From top to bottom, shown are stellar mass surface density, stellar age, [Fe/H], and [Mg/Fe]. Stellar mass increases from left to right. Low-M_h centrals have younger stellar populations at all radii for $M_* > 10^{11}$ $M_\odot$ and higher [Fe/H] at all radii and all M_* than high-M_h centrals.
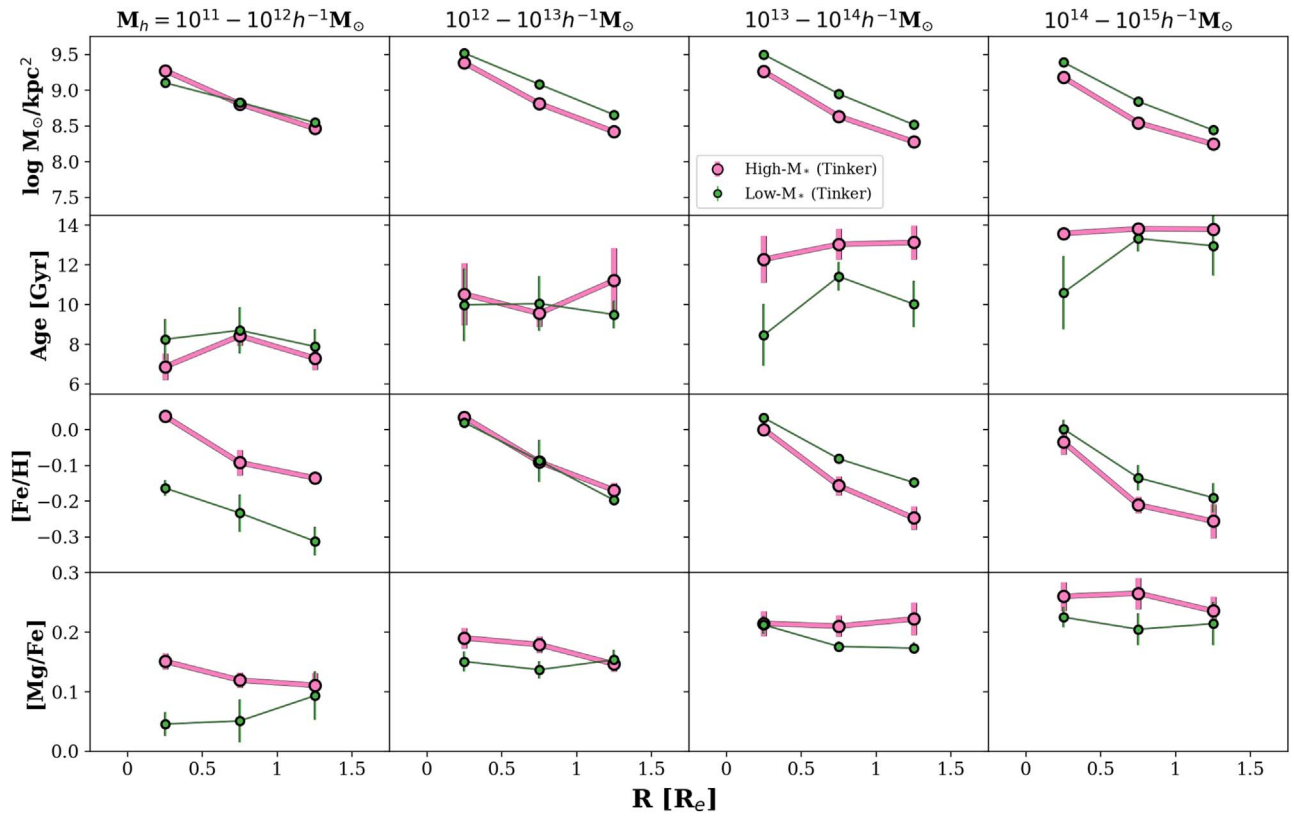
Figure 8. Stellar population profiles of high-M_* (red) and low-M_* (green) centrals at fixed M_h with the Tinker catalog. From top to bottom, shown are stellar mass surface density, stellar age, [Fe/H], and [Mg/Fe]. Stellar mass increases from left to right. Despite their lower Σ_*, high-M_* centrals are more massive owing to their much larger R_e. For $M_h > 10^{12} \, h^{-1} \, M_\odot$, high-$M_*$ centrals have stellar populations that are older, have lower [Fe/H], and show greater [Mg/Fe] than low-M_* centrals at most radii.

shown in Figure 7, with M_* increasing from left to right. High-M_h profiles are shown in blue and low-M_h profiles in orange. The comparison at fixed M_h is shown in Figure 8, with high-M_* centrals in magenta and low-M_* centrals in green. The findings reported in this section apply to both catalogs, although only measurements using the Tinker catalog are shown to keep the figures simple.

In general, the stellar population profiles confirm the differences in normalization that we reported in Figure 5 and Section 4.2. We find stellar population differences to be rather constant with radius, indicating that no significant differences in profile shape are apparent between the subsamples. The stellar age and [Mg/Fe] profiles all tend to be flat, while the [Fe/H] profiles all fall with radius, as reported in previous work (e.g., Greene et al. 2015; van Dokkum et al. 2017; Alton et al. 2018; Parikh et al. 2018, 2019, 2021; Zheng et al. 2019; Lacerna et al. 2020).

The fact that parameter differences are mostly constant with radius indicates that the results in the integrated properties are not driven by outlier radial bins. This could have been more problematic in the outskirts, where the spectral S/N is a factor of two lower than at the centers (see the Appendix). The profiles would also reveal whether any trends in the integrated measurements are driven by standout physical behavior. For example, recent central star formation could also lower the mass-weighted stellar ages at the center, but we see no evidence for this either.

We therefore conclude that any variations in the shape of the stellar population profiles within $1.5R_e$ must be very subtle. Processes like radial migration could contribute to "washing

out" any subtle differences that might have been imparted by past events in the assembly history (Minchev et al. 2012; El-Badry et al. 2016). Moreover, the galactocentric distances probed in this paper are just inward of the radii at which the stellar metallicity profiles of nearby galaxies start to show flattening due to minor mergers and stellar accretion from satellite galaxies (Oyarzún et al. 2019).

5. Discussion

5.1. How Halo Mass Modulates the Stellar Populations of Passive Centrals at Fixed M_*

In the two-phase scenario for galaxy evolution, the in situ formation of central galaxies is followed by a phase of ex situ growth through stellar accretion (Oser et al. 2010, 2012; Johansson et al. 2012b; Moster et al. 2013; Furlong et al. 2017). Recent observations of nearby massive galaxies provide support for this secondary phase. The stellar density profiles of massive galaxies at low redshift have faint, extended stellar envelopes that could have originated from late-time stellar accretion (Huang et al. 2013a, 2013b, 2018), as also identified locally in the Milky Way (e.g., Fernández-Trincado et al. 2019, 2020). Massive nearby galaxies also show flat stellar metallicity profiles beyond the R_e, as would be expected if their outskirts assembled through minor mergers (Oyarzún et al. 2019).

In Oyarzún et al. (2019), we showed that this transition in the shape of the stellar metallicity profiles becomes prominent in galaxies with stellar mass greater than $M_* = 10^{11} \, M_\odot$. Our estimates of the ex situ stellar mass fraction at R_e are consistent

with zero for $M_* < 10^{11}\ M_\odot$ and unity for $M_* > 10^{11}\ M_\odot$. A phase transition around $M_* = 10^{11}\ M_\odot$ also emerges in theoretical predictions. The baryon-to-star conversion efficiency is believed to peak around $M_* = 10^{10.5}\ M_\odot$ (e.g., Behroozi et al. 2013; Girelli et al. 2020), thus creating an inflection point in the SHMR (e.g., Moster et al. 2010; Posti & Fall 2021). As M_* increases, the conversion efficiency decreases and mergers grow in importance (Rodriguez-Gomez et al. 2016; Rodríguez-Puebla et al. 2017). To first order, stellar mass that would have formed in the central galaxy at lower masses becomes increasingly locked up in satellites and the "intragroup" medium of host halos at higher masses. We can use these insights to inform our interpretation of Figures 5 and 7.

Focusing on lower-mass galaxies with $M_* < 10^{11}\ M_\odot$, we see that centrals in low-M_h halos have higher [Fe/H] within $1.5R_e$ than centrals with the same M_* in larger halos. The same trend was recovered by Greene et al. (2015) in the MASSIVE survey (Greene et al. 2013; though we should note that the opposite result was found by La Barbera et al. 2014 and Rosani et al. 2018; more in Section 5.2.3). This result can be interpreted two ways. First, it might imply that central galaxies in high-M_h halos more efficiently retained their gas throughout their star formation episodes. This could have led to rapid star formation, therefore enhancing their [Mg/Fe], which is precisely what we observe in Section 5. This Mg enhancement in high-M_h centrals was also detected by Scholz-Díaz et al. (2022), who also characterized the stellar populations of central galaxies, but with single-fiber SDSS spectroscopy.

Alternatively, we know by definition that at fixed M_* low-M_h centrals also have higher M_*-to-M_h ratios and lower numbers of satellites (see Figure 2). Perhaps our results are simply a sign of more extended central SFHs at lower halo masses, where lower virial temperatures and fewer satellites allow for longer periods of cold flow accretion (e.g., Dekel & Birnboim 2006; Zu & Mandelbaum 2016).

Before turning to the interpretation of our results toward $M_* > 10^{11}\ M_\odot$, we should emphasize that our sample binning and spectral S/N requirements in this work prevent us from studying the flattening of metallicity profiles in the low surface brightness outskirts of massive galaxies that were the subject of Oyarzún et al. (2019). The profiles in Figure 7 are mostly limited to the inner regions of galaxies, within $\sim 1.5R_e$. That said, we see in this work that M_h has an impact on the formation of passive galaxies, even at the centers of $M_* > 10^{11}\ M_\odot$ centrals. Though subtle, these signatures of halo-modulated evolution are significantly detected, as evidenced in Figures 3 and 4.

For $M_* > 10^{11}\ M_\odot$, the stars in high-M_h halo centrals are older than their counterparts in low-M_h halos. At these large M_*, high-M_h centrals also have lower [Fe/H] and higher [Mg/Fe] at all radii. The fact that these differences are present at the centers and show little radial variation points to differences in in situ formation, as opposed to minor merger accretion at larger radii. In line with our interpretation at lower M_*, a possible explanation is that low-M_h centrals continued forming stars over longer timescales. A later onset of quenching would yield younger stellar ages, higher [Fe/H], and lower [Mg/Fe] as measured today.

Given the more active merger history of high-M_* galaxies, it is worth exploring the possibility that a fraction of the stars at the centers of $M_* > 10^{11}\ M_\odot$ centrals were accreted. To lower the [Fe/H] abundance and increase the stellar age in high-M_h centrals, accreted stars would have to be metal-poor and old.

Oyarzún et al. (2019) argued that signatures of minor mergers are produced by the accretion of stellar envelopes that are more metal-poor than the inner regions of the central, giving credibility to this explanation. However, explaining why accreted stellar populations would be old is more challenging. The stellar ages of satellite galaxies rarely exceed 10 Gyr, even in halos as massive as $M_h > 10^{14}\ h^{-1}\ M_\odot$ (Pasquali et al. 2010). Yet the stellar ages of high-M_h centrals can be as old as 12 Gyr for $M_* = 10^{11.5}\ M_\odot$.

Recently, Huang et al. (2020) exploited deep, wide-field imaging to measure individual ETG surface brightness profiles to $R \sim 150$ kpc for a sample large enough that precise M_h estimates could be derived through galaxy−galaxy weak lensing. They found that, as a function of their host halo M_h, central galaxies contain more M_* not only in their centers but also in their distant outskirts. If dry minor mergers are required to build those outskirts, does this mean that larger halos must be effective in suppressing star formation in both their central galaxies *and* the within-the-satellite population that will later merge onto those centrals? Further exploration of this question requires a direct comparison between the stellar population profiles of central and satellite galaxies, a subject we will return to in future work.

5.2. How M_* Drives Evolution within Dark Matter Halos of Identical Mass

So far, we have discussed the influence of the host dark matter halo mass (M_h) as a secondary, modulating variable in the formation and evolution of passive central galaxies at fixed M_*. This approach follows a long line of literature seeking to understand the role of "environment" after controlling for luminosity or stellar mass (e.g., Dressler 1980; Kauffmann et al. 2004; Peng et al. 2010).

Our theoretical understanding of galaxy formation, however, begins by assuming an underlying distribution of evolving dark matter halos and then seeks to build physical models on top (see Benson et al. 2000; Moster et al. 2013; Somerville & Davé 2015). Acknowledging our imperfect ability in this paper to measure dark matter halos observationally (see Section 5.2.3), we nonetheless turn to a theory-minded perspective, in which halo mass is the primary variable. By studying trends with M_* in bins of fixed M_h, we gain insight into the range of evolution that occurs within halos of fixed mass today.

Considering stellar age, [Fe/H], and [Mg/Fe] in nearly every mass bin, the bottom row of Figure 8 shows that the stellar populations of central galaxies at fixed M_h depend strongly on stellar mass. On the one hand, this result seems to be a familiar expression of how stellar populations depend on the luminosity of ETGs (see Renzini 2006 for a review). But when we remember that our trends are seen at fixed M_h, they are perhaps more surprising. In two halos of identical mass today, central galaxies with different M_* have markedly different formation histories.

We discuss two physical interpretations of this result before concluding the discussion with an examination of potential observational biases.

5.2.1. Varying Conditions of Early Formation

Our first interpretation follows in the spirit of "monolithic collapse," namely, that the early conditions ($z \sim 4$) for gas accretion and mergers determine how the vast majority of stars

in ETGs form. Rapid, intense formation leads to a greater stellar mass content (van Dokkum et al. 2009; Newman et al. 2010; Damjanov et al. 2011; Whitaker et al. 2012; Dekel & Burkert 2014; Zolotov et al. 2015). The number of stars formed in this early phase may therefore be largely independent of the progenitor halo properties, let alone the halo's final mass at $z = 0$.

In this picture, certain halos would happen to host the conditions needed for gas-rich mergers that promote the early formation of massive central galaxies. These events would have to rapidly exhaust gas supplies to produce old and chemically enriched stellar populations today. Unfortunately, testing this scenario with stellar population profiles is challenging because the imprint of gas-rich mergers is hard to predict and sensitive to the initial conditions of the encounter (Kobayashi 2004).

We note, however, that at all M_h high-M_* centrals are larger in size and show higher Σ_* [$M_\odot$/kpc] within $\sim 1 R_e$ compared to their low-M_* counterparts (see Figure 8). Their initial "collapse" may have driven up such large central gas densities that the resulting deep potential wells limited the impact of feedback, driving runaway growth in M_* (e.g., Matteucci 1994; Wellons et al. 2015). Such a period of collapse might leave kinematic and morphological signatures. Gas-rich major mergers might preserve the spin of the merger remnant, for example, giving rise to compact disks at $z \sim 2$ (e.g., van der Wel et al. 2011) and so-called fast rotators (e.g., Graham et al. 2018). On the other hand, a more extended formation period followed by dry mergers might produce slow rotator galaxies (Naab et al. 2014).

In a sense, this general picture aligns with Section 5.1 in that stellar mass, and not the dark matter halo, emerges as the dominant variable that controls how the bulk of stars in passive centrals form. This would seem antithetical to current theoretical models, however, and inconsistent with a variety of observational studies emphasizing the importance of M_h, or at least proxies thereof (e.g., $\Sigma_{1\,kpc}$ and σ_*), in driving galaxy properties (Figures 3 and 4 of this paper and, e.g., Franx et al. 2008; Wake et al. 2012; Chen et al. 2020; Estrada-Carpenter et al. 2020).

5.2.2. Galaxy Assembly Bias

If a galaxy's growth history is ultimately tied to its dark matter halo, then Figure 5 tells us that other halo parameters, beyond M_h, must play a role. These might include halo formation time and halo clustering (e.g., Gao et al. 2005; Wechsler et al. 2006), secondary properties that invoke the idea of "halo assembly bias." By definition, this term encapsulates all correlations between halo clustering and the assembly histories of halos at fixed M_h (Mao et al. 2018; Mansfield & Kravtsov 2020). For example, dark matter halos that assembled early tend to be more strongly clustered than counterparts that assembled at lower redshift (Gao et al. 2005; Contreras et al. 2019), especially for $M_h < 10^{13}\ h^{-1}\ M_\odot$ (Li et al. 2008).

The strong statistical relationship between halos and the galaxies they host (e.g., Leauthaud et al. 2017) has motivated predictions for how halo assembly bias might impact galaxy formation. Croton et al. (2007) used semianalytic models to predict that halo formation time should correlate with galaxy luminosity at fixed M_h. In a halo mass bin of $M_h = 10^{14} - 10^{15.5}\ h^{-1}\ M_\odot$, they found that bright centrals formed in those halos that had mostly assembled by $z \sim 1$, whereas fainter centrals were associated with halos that assembled later ($z \sim 0.5$). Zehavi et al. (2018) expanded

on this result, predicting a dependence of central M_* on halo formation time at fixed M_h.

An implied secondary dependence of stellar mass growth on halo age has also been studied with semiempirical models. Bradshaw et al. (2020), for example, report factor of ~ 3 differences in "central" M_* between the 20% youngest and oldest halos at fixed halo mass above $M_h > 10^{13}\ M_\odot$ as modeled in the UniverseMachine (UM; Behroozi et al. 2019). This difference in M_* and age (of approximately 1–2 Gyr) is similar to our results in the two bottom left panels of Figure 5.

A galaxy assembly bias signal is also predicted in cosmological hydrodynamic simulations like EAGLE (Crain et al. 2015; Schaye et al. 2015; Matthee et al. 2017; Kulier et al. 2019) and Illustris (Vogelsberger et al. 2014; Nelson et al. 2015; Xu & Zheng 2020), where it is driven by the fact that halos in dense regions not only collapse earlier but also do so with higher halo concentrations (e.g., Wechsler et al. 2002; Zhao et al. 2009; Correa et al. 2015; Hearin et al. 2016b). That yields deeper potential wells (Matthee et al. 2017) and more efficient central star formation (e.g., Booth & Schaye 2010). For example, Matthee et al. (2017) found an order-of-magnitude variation in central M_* at fixed halo mass below $M_h \lesssim 10^{12}\ M_\odot$. This variation correlates strongly with halo assembly time, which spans $z = 0.6$–3 (see their Figure 7).

In IllustrisTNG, galaxy assembly bias is strongly imprinted in galaxy observables. At fixed M_h, central galaxies that are dispersion dominated, are redder, are larger, and have higher M_* are more strongly clustered, especially for $M_h < 10^{13}\ h^{-1}$ $M_\odot$ (Montero-Dorta et al. 2020). In addition, centrals in IllustrisTNG with high M_*-to-M_h ratios exhausted their gas reservoirs earlier, thus quenching at higher redshifts (Montero-Dorta et al. 2021).

It is tempting to map these predictions to our observational results. At fixed M_h, high-M_* centrals have stellar populations that are older, have higher [Mg/Fe], and show lower [Fe/H], revealing that they formed earlier and more rapidly. In the galaxy assembly bias scenario, this is a consequence of galaxy formation in older, highly concentrated halos. This explanation was also proposed by Scholz-Díaz et al. (2022) to explain why the same trends for stellar age and [Mg/Fe] are present in single-fiber spectra from SDSS.

Before we consider observational biases on this conclusion (Section 5.2.3), it is worth noting that there is disagreement among theoretical predictions for the detailed behavior of galaxy assembly bias. In the UM analysis, the secondary correlation with halo formation time is strongest for $M_h \gtrsim 10^{14}$ $M_\odot$ (Bradshaw et al. 2020; see also Croton et al. 2007). But Matthee et al. (2017) find that halo formation time in EAGLE has no effect above $M_h \gtrsim 10^{12}\ M_\odot$, instead strengthening at lower masses (see also Kulier et al. 2019). Meanwhile, Zehavi et al. (2018) and Xu & Zheng (2020) find a correlation between halo age and M_* that peaks around $M_h \sim 10^{12}\ h^{-1}\ M_\odot$ and mildly decreases in significance toward $M_h \gtrsim 10^{13.5}\ h^{-1}\ M_\odot$. Uncertainties in late-time growth explain some of the discrepancy. In hydrodynamical simulations, the stochasticity of late mergers can wash out formation-time bias at high M_h (Matthee et al. 2017). The opposite happens in the UM because the bias here is driven by accreted stellar populations (Bradshaw et al. 2020). Halo age primarily influences the stellar mass that was accreted through mergers rather than the populations formed in situ.

Finally, we note that the more rapid formation of high-M_* centrals, as inferred from the [Mg/Fe] and [Fe/H] measurements, is in agreement with the analysis by Montero-Dorta et al. (2021) in IllustrisTNG. However, it is in contrast with how high-M_* centrals assemble in EAGLE, where they grow by forming stars over long timescales (Kulier et al. 2019). As Contreras et al. (2021) concluded in their comparison of different galaxy assembly bias models, the amplitude and behavior of the signal are strongly model dependent.

5.2.3. Systematic Errors and Assembly Bias Signal

Many studies have searched for signatures of galaxy assembly bias, and tentative detections have been reported, including correlations between halo concentration and the occupation fraction of centrals (Zentner et al. 2019; Lehmann et al. 2017), spatial clustering of galaxies (e.g., Berlind et al. 2006; Lacerna et al. 2014; Montero-Dorta et al. 2017), and galactic "conformity" (i.e., similarity in the physical properties of galaxies within a halo; Weinmann et al. 2006; Hearin et al. 2016a; Berti et al. 2017; Calderon et al. 2018; Mansfield & Kravtsov 2020). Unfortunately, systematic errors in the distinction between centrals and satellites, halo mass estimates, and other problems have called into question many of these results (see Campbell et al. 2015; Lin et al. 2016; Tinker et al. 2018; Wechsler & Tinker 2018).

Much of the concern in our work centers on the group catalogs we use to infer the host dark matter halo properties. Indeed, we show explicitly that the choice of group catalog can affect our results. For example, the Yang+Wang and Tinker catalogs disagree as to whether low-M_h centrals have higher or lower [Fe/H] than their high-M_h counterparts (see Figure 5). These discrepancies are also present in other work. La Barbera et al. (2014) and Rosani et al. (2018) used the Yang et al. (2007) catalog to find that high-M_h centrals have younger and more iron-enriched populations than low-M_h centrals. The opposite was found by Greene et al. (2015) with the catalog by Crook et al. (2007).

While we favor the new group catalogs from Tinker (2020, 2021), which are more sophisticated, self-consistent, and robust thanks to deeper imaging, systematic errors in M_h may significantly impact our conclusions. This is in large part because the M_h estimates *depend*, at least in part, on the M_* of the central galaxy. In addition to counting satellite luminosity, the Tinker catalog also employs color and r-band light concentration when assigning M_h to an associated central galaxy. Our results indicate that high-M_* centrals have higher central Σ_*, the opposite of the expected bias with concentration. But they do have fewer satellites (apparent in Figure 2). This is expected because the central and satellite M_* values must roughly add to a constant at fixed M_h. It is possible that the history of satellite accretion drives the stellar population trends we see, independently of the halo assembly history.

Finally, the identified sample of "central" galaxies (which is roughly identical in the Tinker and Yang+Wang catalogs) is both incomplete and contaminated (by actual satellite galaxies) in ways that likely depend on M_* and inferred M_h. Disentangling these effects requires substantial mock observations that are beyond the scope of this paper.

Instead, in future work we can make progress by measuring observables associated with our subsamples that are independent of galaxy luminosity (i.e., independent of M_*). For example, the assembly bias interpretation would be strengthened by a detection of different large-scale density signals on 10 Mpc scales for high- versus low-M_* galaxies at fixed M_h. Likewise, we can exploit new, more accurate proxies for M_h (e.g., Bradshaw et al. 2020), eventually aiming to derive M_h estimates from stacked weak lensing.

6. Summary

We constructed a sample of over 2200 passive central galaxies from the MaNGA survey to study how their assembly histories depend on M_* and M_h. We constrained the stellar populations of our galaxies to high precision through spectral stacking and characterization with the codes Prospector and alf. We also control for systematics in M_h estimation by comparing the outputs from the group catalogs by Yang et al. (2007), Wang et al. (2016), and Tinker (2020, 2021). Our findings can be summarized as follows:

1. At fixed M_*, there are significant differences in the spectra of passive centrals as a function of M_h. These differences are present at all M_* and we detect them at all radii ($R < 1.5R_e$). With no modeling involved, this shows that host halos have an impact on the formation of central galaxies.

2. To associate these spectral differences with stellar population variations, we turned to fitting with Prospector and alf. At fixed M_*, centrals in more massive halos show older stellar ages, lower [Fe/H], and higher [Mg/Fe]. A possible explanation for this result is that centrals in massive halos more efficiently retained their gas, allowing for early and rapid formation. Alternatively, the fewer satellites in low-M_h centrals could allow for longer periods of cold flow accretion onto the central galaxy, resulting in more extended SFHs.

3. At fixed M_h, centrals with high M_* have older stellar populations and formed in shorter timescales (low [Fe/H] and high [Mg/Fe]) than centrals with low M_*. At first glance, this result might be expected given how the stellar populations of ETGs depend on M_*. However, our results are among the first to distinguish these evolutionary trends at fixed M_h. We propose two different scenarios to explain these results:

Varying conditions of early formation: at fixed M_h, centrals that undergo gas-rich mergers can fuel rapid, intense star formation episodes followed by runaway growth in M_*. This process of "enhanced collapse" leads to the formation of old, α-enhanced stellar populations.

Galaxy assembly bias: according to theory, central galaxies with high M_*-to-M_h ratios assembled in early-forming, highly concentrated halos. Their gravitational potentials lead to early star formation, efficient metal retention, and rapid exhaustion of their gas reservoirs.

4. Though we use two group catalogs in our analysis, we are still sensitive to sample contamination and systematic errors in M_h estimation. Future work can improve on these difficulties by measuring observables that are independent of galaxy luminosity or by exploiting more accurate proxies for M_h.

Appendix
Model Fits and Posterior Distributions

Figures A1, A2, A3, and A4 show some of the fits and composite posterior distributions for high-M_* (red) and low-M_* (green) centrals. Halo mass increases with figure number. Top panels show the continuum-subtracted stacks and best fits. Residuals are plotted underneath. The errors shown in gray include the jitter and inflated error terms implemented by alf. Black vertical lines delimit the wavelength ranges used for continuum subtraction.

The bottom panels show the posterior distributions of mass-weighted ages, [Fe/H], and [Mg/Fe] derived with alf for the two corresponding spectra. The assumptions used to derive these quantities from raw alf outputs are described in Section 3.5. We fitted for a two-component SFH, stellar velocity dispersion, IMF, and the abundances of 19 elements. Posterior sampling was performed with emcee (Foreman-Mackey et al. 2013).
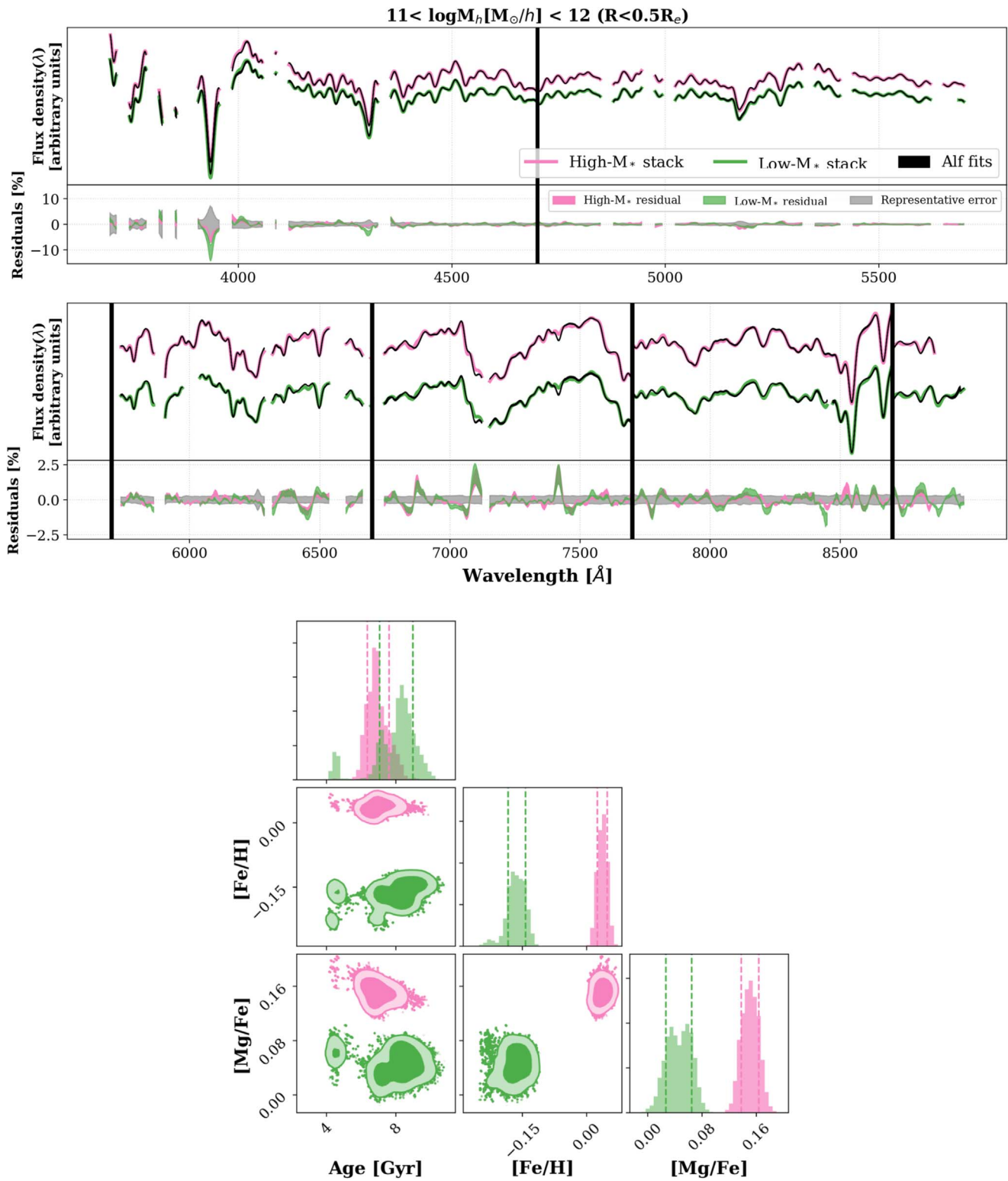
Figure A1. Top: best fits and residuals for the $11 < \log M_h[M_\odot/h] < 12$ bin ($R < 0.5R_e$). Bottom: posterior distributions. Details are given in the Appendix.
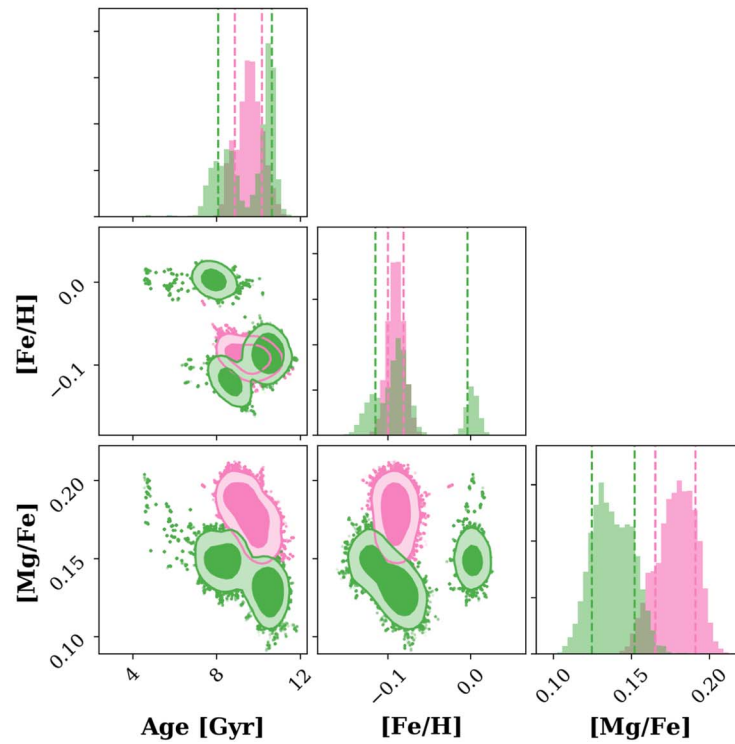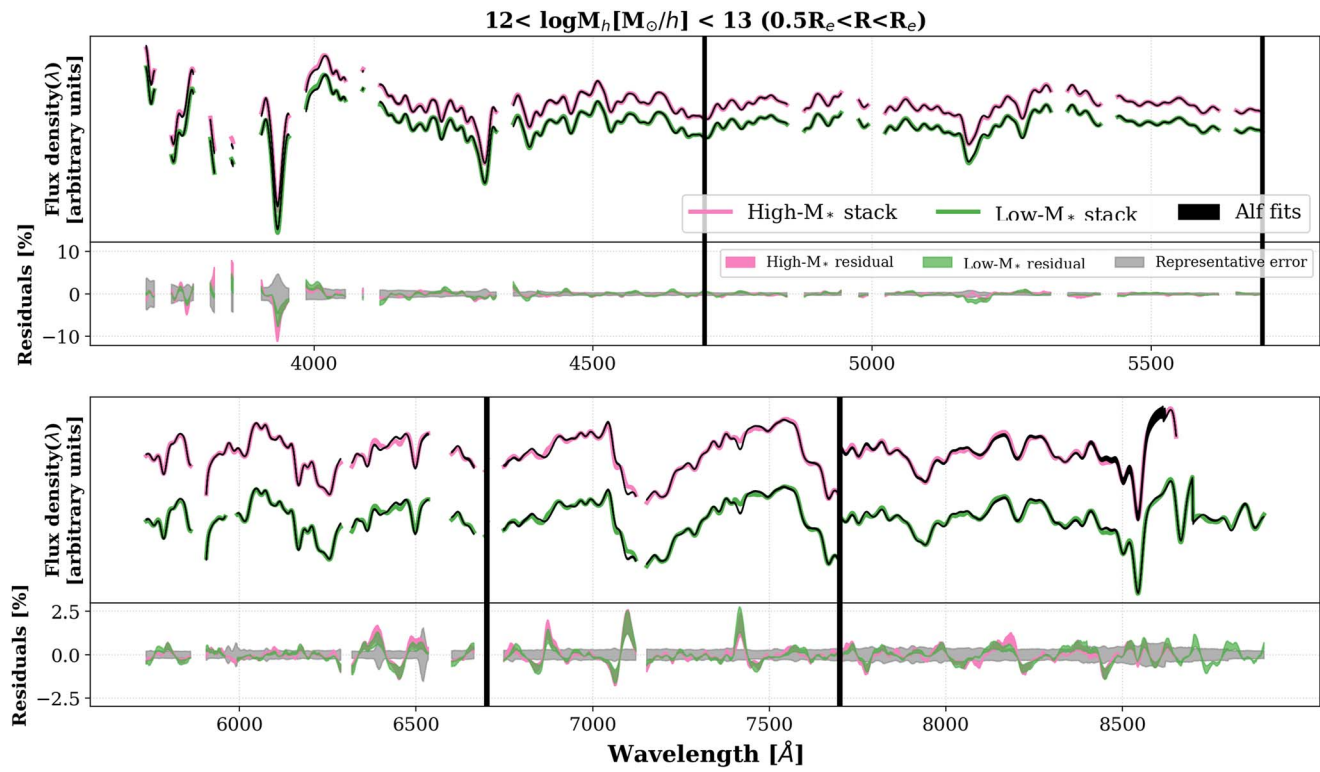
Figure A2. Top: best fits and residuals for the $12 < \log M_h[M_\odot/h] < 13$ bin ($0.5R_e < R < R_e$). Bottom: posterior distributions. Details are given in the Appendix.
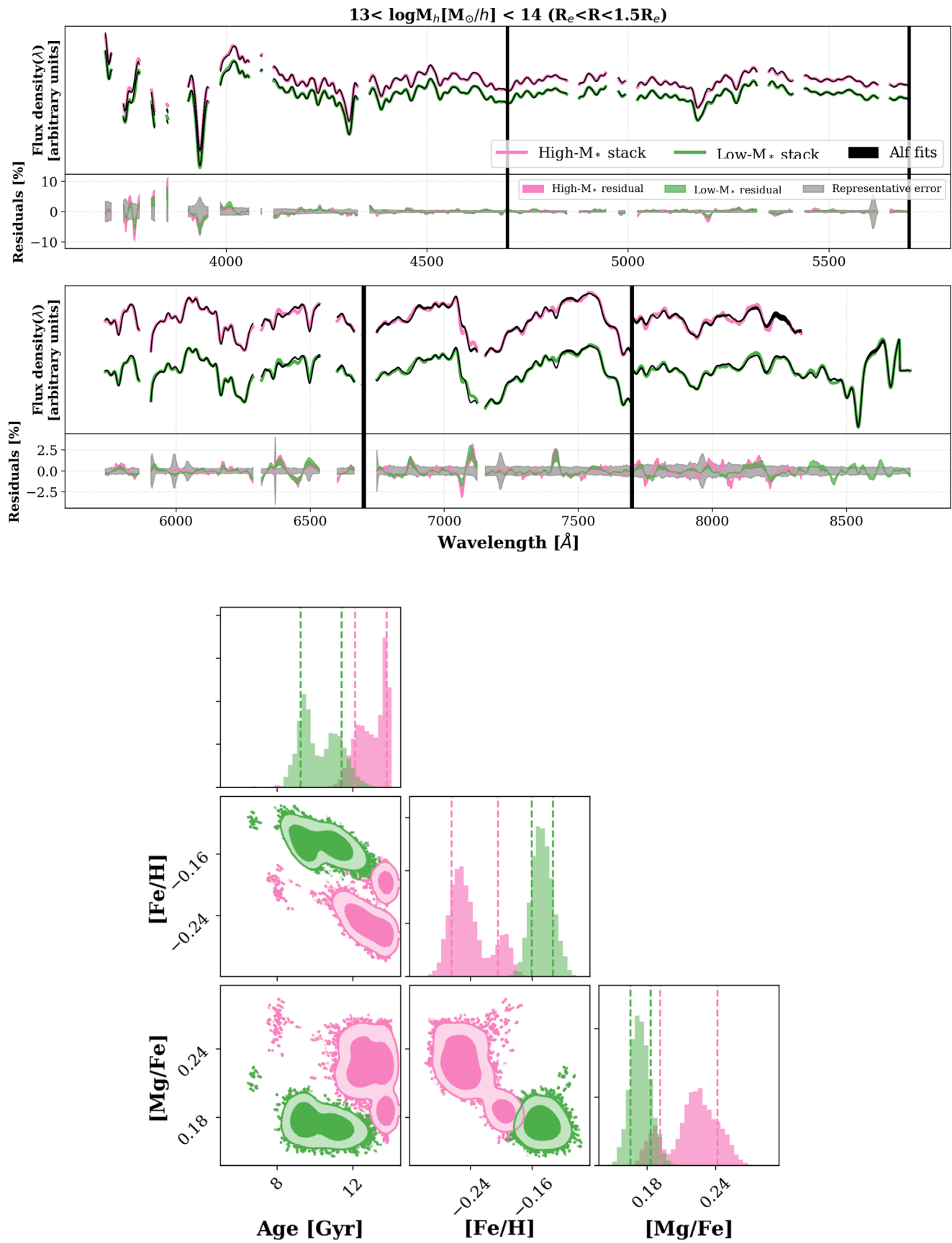
Figure A3. Top: best fits and residuals for the $13 < \log M_h[M_\odot/h] < 14$ bin ($R_e < R < 1.5 R_e$). Bottom: posterior distributions. Details are given in the Appendix.
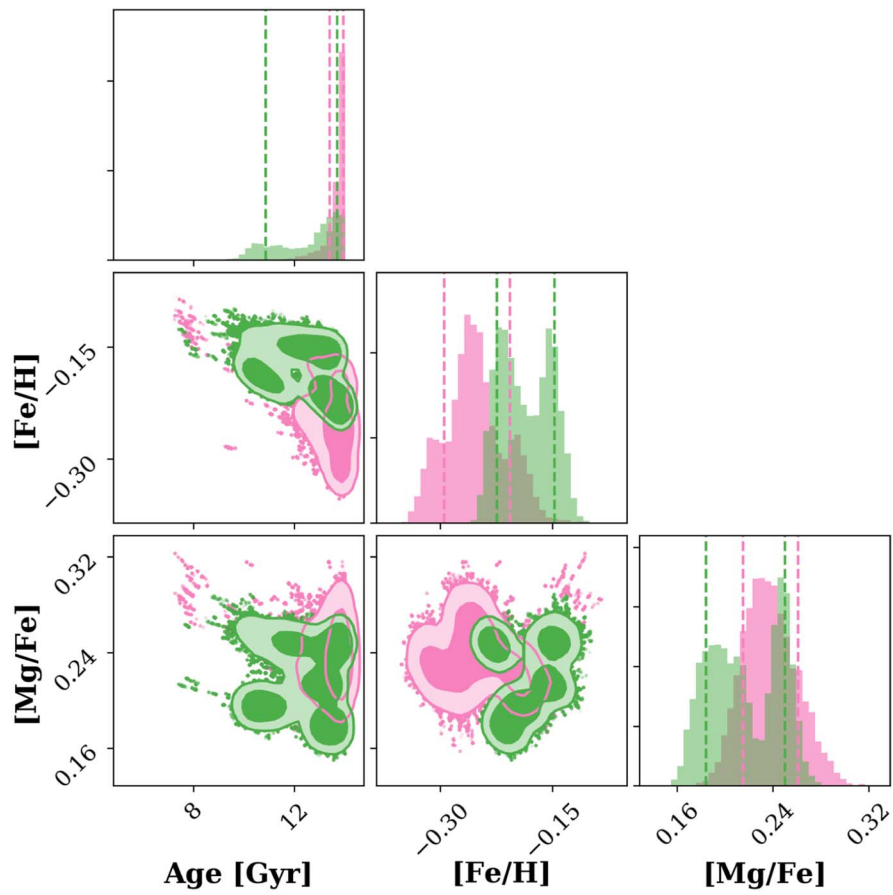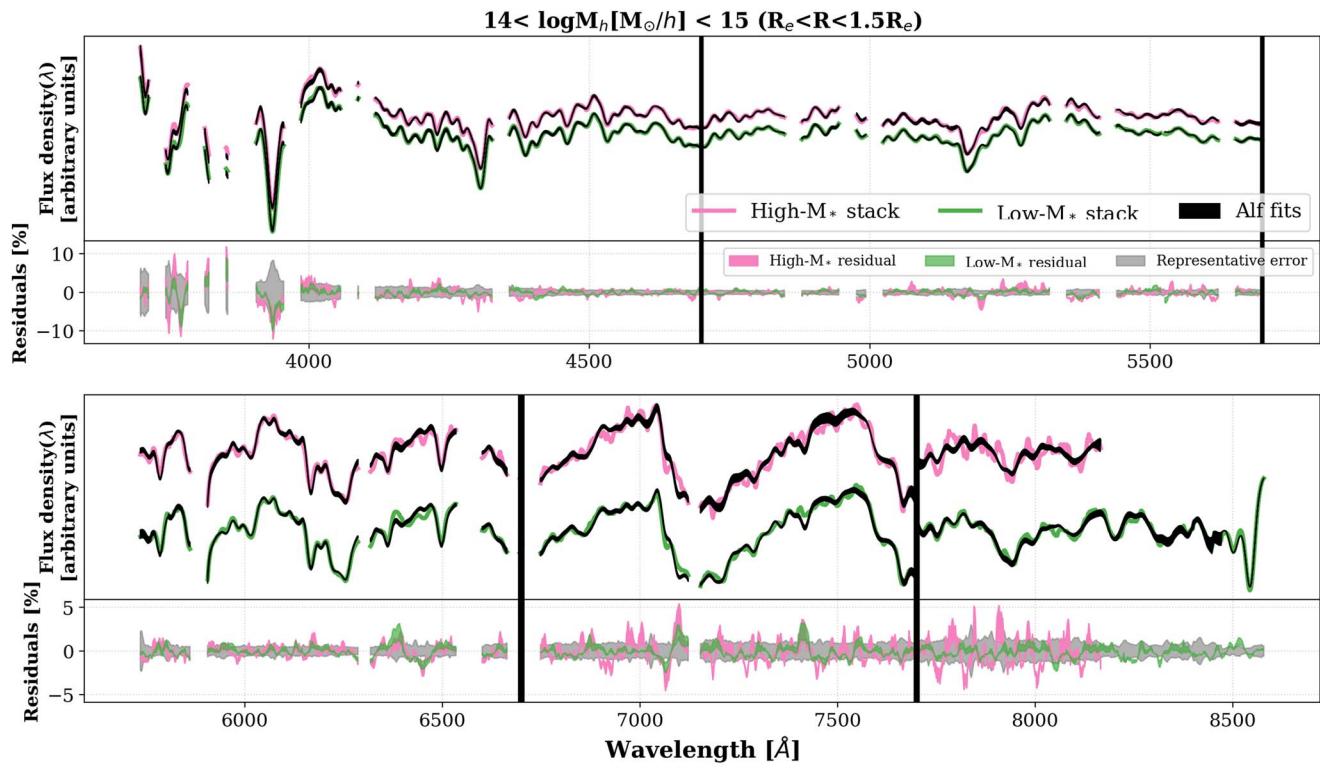
Figure A4. Top: best fits and residuals for the $14 < \log M_h[M_\odot/h] < 15$ bin ($R_e < R < 1.5R_e$). Bottom: posterior distributions. Details are given in the Appendix.

ORCID iDs

Grecco A. Oyarzún ⓘ https://orcid.org/0000-0003-0028-4130
Kevin Bundy ⓘ https://orcid.org/0000-0001-9742-3138
Kyle B. Westfall ⓘ https://orcid.org/0000-0003-1809-6920
Jeremy L. Tinker ⓘ https://orcid.org/0000-0003-3578-6149
Francesco Belfiore ⓘ https://orcid.org/0000-0002-2545-5752
Maria Argudo-Fernández ⓘ https://orcid.org/0000-0002-0789-2326
Charlie Conroy ⓘ https://orcid.org/0000-0002-1590-8551
Karen L. Masters ⓘ https://orcid.org/0000-0003-0846-9578
David Wake ⓘ https://orcid.org/0000-0002-6047-1010
David R. Law ⓘ https://orcid.org/0000-0002-9402-186X
Richard M. McDermid ⓘ https://orcid.org/0000-0002-8175-7229
Alfonso Aragón-Salamanca ⓘ https://orcid.org/0000-0001-8215-1256
Renbin Yan ⓘ https://orcid.org/0000-0003-1025-1711
Matthew Bershady ⓘ https://orcid.org/0000-0002-3131-4374
Sebastián F. Sánchez ⓘ https://orcid.org/0000-0001-6444-9307
Brett H. Andrews ⓘ https://orcid.org/0000-0001-8085-5890
Richard R. Lane ⓘ https://orcid.org/0000-0003-1805-0316
D. Bizyaev ⓘ https://orcid.org/0000-0002-3601-133X
Ivan Lacerna ⓘ https://orcid.org/0000-0002-7802-7356
J. R. Brownstein ⓘ https://orcid.org/0000-0002-8725-1069
Niv Drory ⓘ https://orcid.org/0000-0002-7339-3170
Kai Zhang ⓘ https://orcid.org/0000-0002-9808-3646

References

Adelman-McCarthy, J. K., Agüeros, M. A., Allam, S. S., et al. 2006, ApJS, 162, 38
Aguado, D. S., Ahumada, R., Almeida, A., et al. 2019, ApJS, 240, 23
Alam, S., Albareti, F. D., Allende Prieto, C., et al. 2015, ApJS, 219, 12
Allen, J. T., Croom, S. M., Konstantopoulos, I. S., et al. 2015, MNRAS, 446, 1567
Alton, P. D., Smith, R. J., & Lucey, J. R. 2018, MNRAS, 478, 4464
Argudo-Fernández, M., Verley, S., Bergond, G., et al. 2015, A&A, 578, A110
Arimoto, N., & Yoshii, Y. 1987, A&A, 173, 23
Barro, G., Faber, S. M., Pérez-González, P. G., et al. 2013, ApJ, 765, 104
Behroozi, P., Wechsler, R. H., Hearin, A. P., & Conroy, C. 2019, MNRAS, 488, 3143
Behroozi, P. S., Wechsler, R. H., & Conroy, C. 2013, ApJL, 762, L31
Belfiore, F., Westfall, K. B., Schaefer, A., et al. 2019, AJ, 158, 160
Benson, A. J., Cole, S., Frenk, C. S., Baugh, C. M., & Lacey, C. G. 2000, MNRAS, 311, 793
Berlind, A. A., Kazin, E., Blanton, M. R., et al. 2006, arXiv:astro-ph/0610524
Bernardi, M., Meert, A., Sheth, R. K., et al. 2013, MNRAS, 436, 697
Berti, A. M., Coil, A. L., Behroozi, P. S., et al. 2017, ApJ, 834, 87
Bezanson, R., van Dokkum, P. G., Tal, T., et al. 2009, ApJ, 697, 1290
Blanton, M. R., Bershady, M. A., Abolfathi, B., et al. 2017, AJ, 154, 28
Blanton, M. R., Kazin, E., Muna, D., Weaver, B. A., & Price-Whelan, A. 2011, AJ, 142, 31
Blanton, M. R., & Roweis, S. 2007, AJ, 133, 734
Blanton, M. R., Schlegel, D. J., Strauss, M. A., et al. 2005, AJ, 129, 2562
Bluck, A. F. L., Maiolino, R., Sánchez, S. F., et al. 2020, MNRAS, 492, 96
Booth, C. M., & Schaye, J. 2010, MNRAS, 405, L1
Bradshaw, C., Leauthaud, A., Hearin, A., Huang, S., & Behroozi, P. 2020, MNRAS, 493, 337
Bressan, A., Chiosi, C., & Fagotto, F. 1994, ApJS, 94, 63
Buitrago, F., Trujillo, I., Conselice, C. J., et al. 2008, ApJL, 687, L61
Bundy, K., Bershady, M. A., Law, D. R., et al. 2015, ApJ, 798, 7
Calderon, V. F., Berlind, A. A., & Sinha, M. 2018, MNRAS, 480, 2031
Campbell, D., van den Bosch, F. C., Hearin, A., et al. 2015, MNRAS, 452, 444
Cappellari, M. 2017, MNRAS, 466, 798
Cappellari, M., & Emsellem, E. 2004, PASP, 116, 138
Cappellari, M., McDermid, R. M., Alatalo, K., et al. 2013, MNRAS, 432, 1862
Cassata, P., Giavalisco, M., Guo, Y., et al. 2010, ApJL, 714, L79
Cassata, P., Giavalisco, M., Guo, Y., et al. 2011, ApJ, 743, 96
Chen, Z., Faber, S. M., Koo, D. C., et al. 2020, ApJ, 897, 102
Cherinka, B., Andrews, B. H., Sánchez-Gallego, J., et al. 2019, AJ, 158, 74

Choi, J., Dotter, A., Conroy, C., et al. 2016, ApJ, 823, 102
Cid Fernandes, R., Mateus, A., Sodré, L., Stasińska, G., & Gomes, J. M. 2005, MNRAS, 358, 363
Cimatti, A., Cassata, P., Pozzetti, L., et al. 2008, A&A, 482, 21
Conroy, C. 2013, ARA&A, 51, 393
Conroy, C., Graves, G. J., & van Dokkum, P. G. 2014, ApJ, 780, 33
Conroy, C., & Gunn, J. E. 2010, ApJ, 712, 833
Conroy, C., Gunn, J. E., & White, M. 2009, ApJ, 699, 486
Conroy, C., & van Dokkum, P. 2012, ApJ, 747, 69
Conroy, C., Villaume, A., van Dokkum, P. G., & Lind, K. 2018, ApJ, 854, 139
Contini, E., Gu, Q., Kang, X., Rhee, J., & Yi, S. K. 2019, ApJ, 882, 167
Contreras, S., Angulo, R. E., & Zennaro, M. 2021, MNRAS, 504, 5205
Contreras, S., Zehavi, I., Padilla, N., et al. 2019, MNRAS, 484, 1133
Cook, B. A., Conroy, C., Pillepich, A., Rodriguez-Gomez, V., & Hernquist, L. 2016, ApJ, 833, 158
Cooper, A. P., Parry, O. H., Lowing, B., Cole, S., & Frenk, C. 2015, MNRAS, 454, 3185
Correa, C. A., Wyithe, J. S. B., Schaye, J., & Duffy, A. R. 2015, MNRAS, 450, 1521
Crain, R. A., Schaye, J., Bower, R. G., et al. 2015, MNRAS, 450, 1937
Crook, A. C., Huchra, J. P., Martimbeau, N., et al. 2007, ApJ, 655, 790
Croton, D. J., Gao, L., & White, S. D. M. 2007, MNRAS, 374, 1303
Daddi, E., Renzini, A., Pirzkal, N., et al. 2005, ApJ, 626, 680
Damjanov, I., Abraham, R. G., Glazebrook, K., et al. 2011, ApJL, 739, L44
Damjanov, I., McCarthy, P. J., Abraham, R. G., et al. 2009, ApJ, 695, 101
Dekel, A., & Birnboim, Y. 2006, MNRAS, 368, 2
Dekel, A., & Burkert, A. 2014, MNRAS, 438, 1870
Dey, A., Schlegel, D. J., Lang, D., et al. 2019, AJ, 157, 168
Dotter, A. 2016, ApJS, 222, 8
Dressler, A. 1980, ApJ, 236, 351
Drory, N., MacDonald, N., Bershady, M. A., et al. 2015, AJ, 149, 77
Dunkley, J., Komatsu, E., Nolta, M. R., et al. 2009, ApJS, 180, 306
Eggen, O. J., Lynden-Bell, D., & Sandage, A. R. 1962, ApJ, 136, 748
El-Badry, K., Wetzel, A., Geha, M., et al. 2016, ApJ, 820, 131
Estrada-Carpenter, V., Papovich, C., Momcheva, I., et al. 2020, ApJ, 898, 171
Faber, S. M., Friel, E. D., Burstein, D., & Gaskell, C. M. 1985, ApJS, 57, 711
Faber, S. M., & Jackson, R. E. 1976, ApJ, 204, 668
Fernández-Trincado, J. G., Beers, T. C., & Minniti, D. 2020, A&A, 644, A83
Fernández-Trincado, J. G., Beers, T. C., Placco, V. M., et al. 2019, ApJL, 886, L8
Foreman-Mackey, D., Hogg, D. W., Lang, D., & Goodman, J. 2013, PASP, 125, 306
Franx, M., van Dokkum, P. G., Förster Schreiber, N. M., et al. 2008, ApJ, 688, 770
Furlong, M., Bower, R. G., Crain, R. A., et al. 2017, MNRAS, 465, 722
Gallazzi, A., Charlot, S., Brinchmann, J., White, S. D. M., & Tremonti, C. A. 2005, MNRAS, 362, 41
Gao, L., Springel, V., & White, S. D. M. 2005, MNRAS, 363, L66
García-Benito, R., González Delgado, R. M., Pérez, E., et al. 2017, A&A, 608, A27
Girelli, G., Pozzetti, L., Bolzonella, M., et al. 2020, A&A, 634, A135
Goddard, D., Thomas, D., Maraston, C., et al. 2017a, MNRAS, 465, 688
Goddard, D., Thomas, D., Maraston, C., et al. 2017b, MNRAS, 466, 4731
González Delgado, R. M., Cid Fernandes, R., García-Benito, R., et al. 2014, ApJL, 791, L16
Graham, M. T., Cappellari, M., Li, H., et al. 2018, MNRAS, 477, 4711
Greene, J. E., Janish, R., Ma, C.-P., et al. 2015, ApJ, 807, 11
Greene, J. E., Murphy, J. D., Graves, G. J., et al. 2013, ApJ, 776, 64
Gunn, J. E., Siegmund, W. A., Mannery, E. J., et al. 2006, AJ, 131, 2332
Hearin, A. P., Behroozi, P. S., & van den Bosch, F. C. 2016a, MNRAS, 461, 2135
Hearin, A. P., Zentner, A. R., van den Bosch, F. C., Campbell, D., & Tollerud, E. 2016b, MNRAS, 460, 2552
Hopkins, P. F., Bundy, K., Croton, D., et al. 2010a, ApJ, 715, 202
Hopkins, P. F., Bundy, K., Hernquist, L., Wuyts, S., & Cox, T. J. 2010b, MNRAS, 401, 1099
Huang, S., Ho, L. C., Peng, C. Y., Li, Z.-Y., & Barth, A. J. 2013a, ApJ, 766, 47
Huang, S., Ho, L. C., Peng, C. Y., Li, Z.-Y., & Barth, A. J. 2013b, ApJL, 768, L28
Huang, S., Leauthaud, A., Greene, J. E., et al. 2018, MNRAS, 475, 3348
Huang, S., Leauthaud, A., Hearin, A., et al. 2020, MNRAS, 492, 3685
Johansson, J., Thomas, D., & Maraston, C. 2012a, MNRAS, 421, 1908
Johansson, P. H., Naab, T., & Ostriker, J. P. 2012b, ApJ, 754, 115
Johnson, B. D., Leja, J., Conroy, C., & Speagle, J. S. 2021, ApJS, 254, 22
Kauffmann, G., White, S. D. M., Heckman, T. M., et al. 2004, MNRAS, 353, 713

Kirby, E. N., Guhathakurta, P., & Sneden, C. 2008, ApJ, 682, 1217
Klypin, A., Yepes, G., Gottlöber, S., Prada, F., & Heß, S. 2016, MNRAS, 457, 4340
Kobayashi, C. 2004, MNRAS, 347, 740
Kriek, M., & Conroy, C. 2013, ApJL, 775, L16
Kroupa, P. 2001, MNRAS, 322, 231
Kulier, A., Padilla, N., Schaye, J., et al. 2019, MNRAS, 482, 3261
Kurucz, R. L. 2018, in ASP Conf. Ser. 515, Workshop on Astrophysical Opacities (San Francisco, CA: ASP), 47
La Barbera, F., Pasquali, A., Ferreras, I., et al. 2014, MNRAS, 445, 1977
Lacerna, I., Ibarra-Medel, H., Avila-Reese, V., et al. 2020, A&A, 644, A117
Lacerna, I., Padilla, N., & Stasyszyn, F. 2014, MNRAS, 443, 3107
Larson, R. B. 1974, MNRAS, 169, 229
Law, D. R., Cherinka, B., Yan, R., et al. 2016, AJ, 152, 83
Law, D. R., Westfall, K. B., Bershady, M. A., et al. 2021, AJ, 161, 52
Law, D. R., Yan, R., Bershady, M. A., et al. 2015, AJ, 150, 19
Leauthaud, A., Saito, S., Hilbert, S., et al. 2017, MNRAS, 467, 3024
Lehmann, B. V., Mao, Y.-Y., Becker, M. R., Skillman, S. W., & Wechsler, R. H. 2017, ApJ, 834, 37
Leja, J., Carnall, A. C., Johnson, B. D., Conroy, C., & Speagle, J. S. 2019, ApJ, 876, 3
Leja, J., Johnson, B. D., Conroy, C., van Dokkum, P. G., & Byler, N. 2017, ApJ, 837, 170
Li, Y., Mo, H. J., & Gao, L. 2008, MNRAS, 389, 1419
Lin, Y.-T., Mandelbaum, R., Huang, Y.-H., et al. 2016, ApJ, 819, 119
Mansfield, P., & Kravtsov, A. V. 2020, MNRAS, 493, 4763
Mao, Y.-Y., Zentner, A. R., & Wechsler, R. H. 2018, MNRAS, 474, 5143
Matteucci, F. 1994, A&A, 288, 57
Matthee, J., Schaye, J., Crain, R. A., et al. 2017, MNRAS, 465, 2381
McDermid, R. M., Alatalo, K., Blitz, L., et al. 2015, MNRAS, 448, 3484
Minchev, I., Famaey, B., Quillen, A. C., et al. 2012, A&A, 548, A126
Montero-Dorta, A. D., Artale, M. C., Abramo, L. R., et al. 2020, MNRAS, 496, 1182
Montero-Dorta, A. D., Chaves-Montero, J., Artale, M. C., & Favole, G. 2021, MNRAS, 508, 940
Montero-Dorta, A. D., Pérez, E., Prada, F., et al. 2017, ApJL, 848, L2
Moster, B. P., Naab, T., & White, S. D. M. 2013, MNRAS, 428, 3121
Moster, B. P., Somerville, R. S., Maulbetsch, C., et al. 2010, ApJ, 710, 903
Naab, T., Oser, L., Emsellem, E., et al. 2014, MNRAS, 444, 3357
Nelson, D., Pillepich, A., Genel, S., et al. 2015, A&C, 13, 12
Newman, A. B., Ellis, R. S., Treu, T., & Bundy, K. 2010, ApJL, 717, L103
Oke, J. B., & Gunn, J. E. 1983, ApJ, 266, 713
Oser, L., Naab, T., Ostriker, J. P., & Johansson, P. H. 2012, ApJ, 744, 63
Oser, L., Ostriker, J. P., Naab, T., Johansson, P. H., & Burkert, A. 2010, ApJ, 725, 2312
Oyarzún, G. A., Blanc, G. A., González, V., Mateo, M., & Bailey, J. I. I. 2017, ApJ, 843, 133
Oyarzún, G. A., Bundy, K., Westfall, K. B., et al. 2019, ApJ, 880, 111
Parikh, T., Thomas, D., Maraston, C., et al. 2018, MNRAS, 477, 3954
Parikh, T., Thomas, D., Maraston, C., et al. 2019, MNRAS, 483, 3420
Parikh, T., Thomas, D., Maraston, C., et al. 2021, MNRAS, 502, 5508
Pasquali, A., Gallazzi, A., Fontanot, F., et al. 2010, MNRAS, 407, 937
Peng, Y.-j., Lilly, S. J., Kovač, K., et al. 2010, ApJ, 721, 193
Peng, Y.-j., Lilly, S. J., Renzini, A., & Carollo, M. 2012, ApJ, 757, 4
Posti, L., & Fall, S. M. 2021, A&A, 649, A119
Renzini, A. 2006, ARA&A, 44, 141
Rodriguez-Gomez, V., Pillepich, A., Sales, L. V., et al. 2016, MNRAS, 458, 2371
Rodríguez-Puebla, A., Primack, J. R., Avila-Reese, V., & Faber, S. M. 2017, MNRAS, 470, 651
Rosani, G., Pasquali, A., La Barbera, F., Ferreras, I., & Vazdekis, A. 2018, MNRAS, 476, 5233
Salpeter, E. E. 1955, ApJ, 121, 161
Sánchez, S. F., Pérez, E., Sánchez-Blázquez, P., et al. 2016, RMxAA, 52, 171
Sánchez-Blázquez, P., Peletier, R. F., Jiménez-Vicente, J., et al. 2006, MNRAS, 371, 703
Santucci, G., Brough, S., Scott, N., et al. 2020, ApJ, 896, 75
Schaye, J., Crain, R. A., Bower, R. G., et al. 2015, MNRAS, 446, 521
Schiavon, R. P. 2007, ApJS, 171, 146
Scholz-Díaz, L., Martín-Navarro, I., & Falcón-Barroso, J. 2022, MNRAS, 511, 4900
Scott, N., Brough, S., Croom, S. M., et al. 2017, MNRAS, 472, 2833
Smee, S. A., Gunn, J. E., Uomoto, A., et al. 2013, AJ, 146, 32
Somerville, R. S., & Davé, R. 2015, ARA&A, 53, 51
Speagle, J. S. 2020, MNRAS, 493, 3132
Spergel, D. N., Bean, R., Doré, O., et al. 2007, ApJS, 170, 377
Szomoru, D., Franx, M., van Dokkum, P. G., et al. 2013, ApJ, 763, 73
Tange, O. 2018, GNU Parallel 2018 (Ole Tange), v.1, Zenodo, doi:10.5281/zenodo.1146014
Taylor, P., & Kobayashi, C. 2017, MNRAS, 471, 3856
Thomas, D., Maraston, C., Bender, R., & Mendes de Oliveira, C. 2005, ApJ, 621, 673
Thomas, D., Maraston, C., Schawinski, K., Sarzi, M., & Silk, J. 2010, MNRAS, 404, 1775
Tinker, J. L. 2020, arXiv:2007.12200
Tinker, J. L. 2021, ApJ, 923, 154
Tinker, J. L., Hahn, C., Mao, Y.-Y., Wetzel, A. R., & Conroy, C. 2018, MNRAS, 477, 935
Tissera, P. B., Beers, T. C., Carollo, D., & Scannapieco, C. 2014, MNRAS, 439, 3128
Tissera, P. B., Scannapieco, C., Beers, T. C., & Carollo, D. 2013, MNRAS, 432, 3391
Toft, S., van Dokkum, P., Franx, M., et al. 2007, ApJ, 671, 285
Toomre, A. 1977, in Evolution of Galaxies and Stellar Populations, ed. B. M. Tinsley, D. C. Larson, & R. B. Gehret, 401
Tripicco, M. J., & Bell, R. A. 1995, AJ, 110, 3035
Trujillo, I., Conselice, C. J., Bundy, K., et al. 2007, MNRAS, 382, 109
Trujillo, I., Feulner, G., Goranova, Y., et al. 2006a, MNRAS, 373, L36
Trujillo, I., Förster Schreiber, N. M., Rudnick, G., et al. 2006b, ApJ, 650, 18
van den Bosch, F. C., Yang, X., Mo, H. J., et al. 2007, MNRAS, 376, 841
van der Wel, A., Franx, M., van Dokkum, P. G., et al. 2014, ApJ, 788, 28
van der Wel, A., Holden, B. P., Zirm, A. W., et al. 2008, ApJ, 688, 48
van der Wel, A., Rix, H.-W., Wuyts, S., et al. 2011, ApJ, 730, 38
van Dokkum, P., Conroy, C., Villaume, A., Brodie, J., & Romanowsky, A. J. 2017, ApJ, 841, 68
van Dokkum, P. G., Franx, M., Kriek, M., et al. 2008, ApJL, 677, L5
van Dokkum, P. G., Kriek, M., & Franx, M. 2009, Natur, 460, 717
van Dokkum, P. G., Whitaker, K. E., Brammer, G., et al. 2010, ApJ, 709, 1018
Vazdekis, A., Sánchez-Blázquez, P., Falcón-Barroso, J., et al. 2010, MNRAS, 404, 1639
Villaume, A., Conroy, C., Johnson, B., et al. 2017, ApJS, 230, 23
Vogelsberger, M., Genel, S., Springel, V., et al. 2014, MNRAS, 444, 1518
Wake, D. A., Bundy, K., Diamond-Stanic, A. M., et al. 2017, AJ, 154, 86
Wake, D. A., van Dokkum, P. G., & Franx, M. 2012, ApJL, 751, L44
Wang, H., Mo, H. J., Jing, Y. P., et al. 2009, MNRAS, 394, 398
Wang, H., Mo, H. J., Yang, X., et al. 2016, ApJ, 831, 164
Wang, H., Mo, H. J., Yang, X., & van den Bosch, F. C. 2012, MNRAS, 420, 1809
Wechsler, R. H., Bullock, J. S., Primack, J. R., Kravtsov, A. V., & Dekel, A. 2002, ApJ, 568, 52
Wechsler, R. H., & Tinker, J. L. 2018, ARA&A, 56, 435
Wechsler, R. H., Zentner, A. R., Bullock, J. S., Kravtsov, A. V., & Allgood, B. 2006, ApJ, 652, 71
Weinmann, S. M., van den Bosch, F. C., Yang, X., & Mo, H. J. 2006, MNRAS, 366, 2
Wellons, S., Torrey, P., Ma, C.-P., et al. 2015, MNRAS, 449, 361
Wellons, S., Torrey, P., Ma, C.-P., et al. 2016, MNRAS, 456, 1030
Westfall, K. B., Cappellari, M., Bershady, M. A., et al. 2019, AJ, 158, 231
Whitaker, K. E., Kriek, M., van Dokkum, P. G., et al. 2012, ApJ, 745, 179
White, S. D. M., & Rees, M. J. 1978, MNRAS, 183, 341
Worthey, G., Faber, S. M., Gonzalez, J. J., & Burstein, D. 1994, ApJS, 94, 687
Xu, X., & Zheng, Z. 2020, MNRAS, 492, 2739
Yan, R., Bundy, K., Law, D. R., et al. 2016a, AJ, 152, 197
Yan, R., Tremonti, C., Bershady, M. A., et al. 2016b, AJ, 151, 8
Yang, X., Mo, H. J., van den Bosch, F. C., et al. 2007, ApJ, 671, 153
Yang, X., Mo, H. J., van den Bosch, F. C., & Jing, Y. P. 2005, MNRAS, 356, 1293
York, D. G., Adelman, J., Anderson, J. E., Jr., et al. 2000, AJ, 120, 1579
Zehavi, I., Contreras, S., Padilla, N., et al. 2018, ApJ, 853, 84
Zentner, A. R., Hearin, A., van den Bosch, F. C., Lange, J. U., & Villarreal, A. 2019, MNRAS, 485, 1196
Zentner, A. R., Hearin, A. P., & van den Bosch, F. C. 2014, MNRAS, 443, 3044
Zhao, D. H., Jing, Y. P., Mo, H. J., & Börner, G. 2009, ApJ, 707, 354
Zheng, Z., Li, C., Mao, S., et al. 2019, ApJ, 873, 63
Zheng, Z., Wang, H., Ge, J., et al. 2017, MNRAS, 465, 4572
Zirm, A. W., van der Wel, A., Franx, M., et al. 2007, ApJ, 656, 66
Zolotov, A., Dekel, A., Mandelker, N., et al. 2015, MNRAS, 450, 2327
Zolotov, A., Willman, B., Brooks, A. M., et al. 2009, ApJ, 702, 1058
Zu, Y., & Mandelbaum, R. 2016, MNRAS, 457, 4360